Eidgenössische Technische Hochschule Zürich
Swiss Federal Institute of Technology Zurich

Characterizing electromechanical coupling with multiplexed spectroscopy.

Master's Thesis

Yu Yang
yanyu@student.ethz.ch

Laboratory for Solid State Physics
Departement of Physics, D-PHYS
ETH Zürich

Supervisors:
Prof. Dr. Yiwen Chu
Marius Bild
Uwe von Luepke

June 10, 2020

To my parents, my girlfriend He Sun,

My family, and my friends

Thanks to

Prof. Dr. Yiwen Chu

Marius Bild

Uwe von Luepke

For supervising this work

Thanks to Dr. Christopher James Axline for help

Thanks to all group members for the great atmosphere

Abstract

Hybrid quantum systems for coupling superconducting qubits to acoustic quantum states are promising platforms for studying novel approaches to quantum information processing. It has potential in quantum computing, quantum communication, and quantum sensing. In our setup, we utilize bulk acoustic waves (BAW), due to their low loss and orthogonal modes with frequencies in the GHz regime. The properties of these modes are important to our system performance. In this project, we design an experiment to measure these acoustic modes properties. An electrical resonator is designed and coupling to a BAW resonator piezoelectrically. We design using a network analyzer to measure the frequency and phase response of the system. To fit the data and obtain values for the coupling and coherence properties of the involved modes, a model is derived from the basic input-output theory. Experiment parameters are designed based on simulation results. In the experiments performed within the scope of this project, we measured bare electrical resonators and analyzed the data. We also introduce the acoustic resonator based quantum circuit (ARQC) which is to use phonon modes in combination with a superconducting qubit to simulate a quantum circuit. And show a simulation of experiment demonstration which we can realize on our platform based on ARQC. Based on our research, we discuss some application directions of our system and suggest some ways to improve the coupling between the qubit and phonon modes.

Contents

Chapter 1

Introduction

Humans always pursue more powerful computing ability. By Moore's law, the number of transistors on a chip in a dense integrated circuit doubles about every two years [1]. However, during the last decades, this exponential growth starts to saturate. Further reduction in insulator thickness would have resulted in unacceptable and exponential increases in gate leakage current through direct quantum tunneling [2]. Moreover, traditional computers are inefficient in certain important problems, such as prime factorization [3].

Therefore we need to find a new way to achieve more powerful computing, and one of the most attractive solutions is quantum computation [4]. Quantum computation is governed by quantum mechanics. In quantum computation, we no longer use discrete values as 0 and 1 to represent one bit of information, but instead, we use the advantage of superposition and entanglement in quantum mechanics to encode information. Compared with traditional classical computers, quantum computers have a great advantage in searching algorithms, hidden subgroup problems, and quantum simulation. Quantum computation has been developing for decades, both in theory and experiment. Many different physical platforms have so far been investigated for quantum information processing. Examples are superconducting quantum circuits, trapped ions, quantum dots, nuclear magnetic resonance quantum computers, diamond-based quantum computers and so on [5–9]. Each candidate shows their advantages but also shortcomings (e.g. superconducting qubits are easy to scale but have low coherence time, compared to diamond-based quantum computer). We still have a long way to go to achieve a real commercial universal quantum computer.

Besides quantum computation, quantum communication is also a field of growing interest. It is mainly based on the transmission of entangled photon pairs by fiber or in free space. Because of the quantum no-cloning theorem, quantum communication can provide unconditional security, which means a security result is expected to hold against all attacks allowed by quantum mechanics [10]. Satellites utilizing this concept have already been launched and intercontinental quantum communications between China and Austria have been realized [11–13].

Quantum sensing is also a distinct and rapidly growing branch of research within the area of quantum information and has shown significant progress in recent years [14]. Quantum systems and their properties are used to measure physical quantities beyond classical limits. It has higher sensitivity and accuracy and shows great potential value in other fields of science such as biomedical imaging and metrology.

All different branches of quantum information are based on physical implementation.

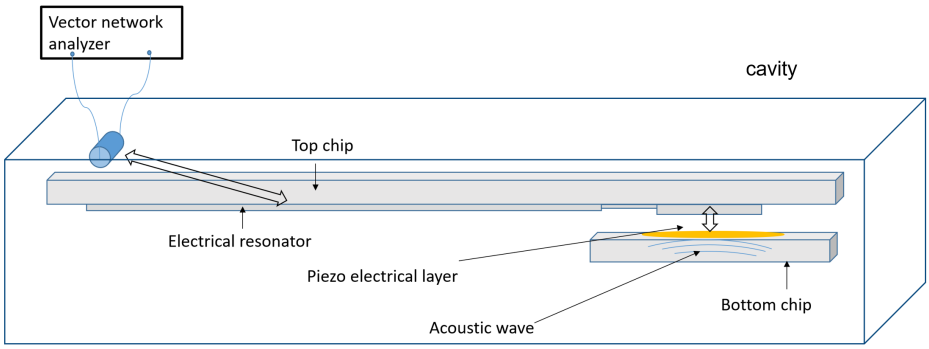

Figure 1.1.: The schematic of the experiment design

Quantum systems normally need well characterized qubits, good coherence, strong two qubit interactions, initialization of the system, fast and high fidelity of readout [15]. However, every system has some disadvantages in several of these properties. The aim of using hybrid quantum systems is to couple different kinds of quantum systems together and combine the advantages of each part [16]. Recently, the coupling of a superconducting qubit and a bulk acoustic resonator has been realized [17, 18]. This hybrid system can take advantage of the long coherence time of the acoustic phonon and controllability of the qubit. This hybrid system shows potential in quantum computation, quantum communication, and quantum sensing. For instance, we could use phonon modes as quantum memories and the qubit as a processor to investigate new models for quantum computation. With this system, we can also realize microwave to optical transduction on the single photon level. We could use this as a single IR photon source but also as a communication link between two superconducting quantum processors.

The purpose of this thesis is to investigate the coupling between qubits and acoustic resonators. In the circuit quantum acoustic dynamics (CQAD) systems, the superconducting qubit is coupled to an acoustic resonator by piezoelectric effect [17, 18]. The properties of the coupling process such as the coupling strength and decay rate of phonon modes determine how many operations can be performed in each sequence of the experiment. Therefore we want to characterize these properties. For simplicity of the measurement and fabrication, we design the device of coupling the acoustic resonator with an electrical resonator to measure these values, which is more convenient in experiment compared to a superconducting qubit.

The schematic of the overall look of the experiment design is shown in Fig 1.1. We print an electrical resonator on one chip. And the acoustic resonator is on another chip. These two resonators are coupled by the piezoelectric effect. The two chips are bonded together and set inside a cavity. There is a pin in the cavity and coupled with the electrical resonator. The pin is connected to a vector network analyzer (VNA) to perform the measurement.

In the second chapter, we will derive a model for our system based on the input-output theory. We begin from the Hamiltonian of our system and the quantum Langevin

equation, combined with the microwave scattering matrix to get the relation between the input signal and the output signal. In the third chapter, we will show the design of each part of the system. The parameters are chosen based on the derived model and the simulation results. In the fourth chapter, we will introduce the fabrication method and measurement setup. We talk about the fabrication of the electrical resonator and acoustic resonator first. The multiplexing setup and dilution fridge setup are introduced afterward. In chapter five, we show the measurement results and data analysis, and we discuss it. In chapter six, we introduce the acoustic resonator based quantum circuit and explain how and why it works. We also simulate a proof-of-principle experiment of this kind of circuit, which we hope to implement on our system. In the last chapter, we make an overall conclusion of the thesis and close with some further outlook on hybrid quantum systems.

Chapter 2

Input-output theory

We want to characterize the properties of acoustic resonators by coupling them to an electrical resonator. The input-output theory is a powerful tool to describe the response of a driven quantum mechanical system. It is applicable to describe transmission or reflection type experiments where an incident pulse is applied to the system and derive the output response of the system to the input field.

2.1. Derivation of input-output theory

We start by computing an electrical resonator coupled to an input-output field. Here, we assume the electrical resonator is the system, the input and output field is the bath [19]. The model can be described by the following Hamiltonian

$$\hat{\mathcal{H}} = \hat{\mathcal{H}}_s + \hat{\mathcal{H}}_b + \hat{\mathcal{H}}_{int}, \tag{2.1}$$

where $\hat{\mathcal{H}}_s$, $\hat{\mathcal{H}}_b$ and $\hat{\mathcal{H}}_{int}$ represent the Hamiltonians of system, bath, and interaction respectively. Currently, we keep the system Hamiltonian generic and use creation and annihilation operators to represent the bath and interaction Hamiltonians. Therefore

$$\hat{\mathcal{H}}_b = \hbar \int_{-\infty}^{\infty} d\omega \omega \hat{b}^+(\omega)\hat{b}(\omega), \tag{2.2}$$

$$\hat{\mathcal{H}}_{int} = \hbar \int_{-\infty}^{\infty} d\omega [\kappa(\omega)\hat{b}^+(\omega)\hat{c} + \kappa^*(\omega)\hat{c}^+\hat{b}(\omega)]. \tag{2.3}$$

Because photons are bosons, which obey Bose-Einstein statistics. So, operator $\hat{b}^+$, $\hat{b}$, which represent the bath field, and $\hat{c}^+$, $\hat{c}$, which represent creation and annihilation operators of the system, have the following commutation relations:

$$[\hat{b}(\omega_1), \hat{b}^+(\omega_2)] = \delta(\omega_1 - \omega_2), \tag{2.4}$$

$$[\hat{c}, \hat{c}^+] = 1. \tag{2.5}$$

In the Heisenberg picture, we obtain the differential equation for the time evolution of the bath field operator:

$$\begin{aligned}\dot{\hat{b}}(\omega) &= \frac{i}{\hbar}[\hat{\mathcal{H}}, \hat{b}(\omega)] \\ &= -i\omega\hat{b}(\omega) + \kappa(\omega)\hat{c}.\end{aligned} \tag{2.6}$$

The evolution of the system field is

$$\begin{aligned}\dot{\hat{c}} &= \frac{i}{\hbar}[\hat{\mathcal{H}}, \hat{c}] \\ &= \frac{i}{\hbar}[\hat{\mathcal{H}}_s, \hat{c}] + \int_{-\infty}^{\infty} d\omega\kappa(\omega)(-\hat{b}(\omega)).\end{aligned} \tag{2.7}$$

Integrating Eq. (2.6), then we get

$$\hat{b}(\omega) = e^{-i\omega(t-t_0)}\hat{b}_0(\omega) + \kappa(\omega)\int_{t_0}^{t} dt' e^{-i\omega(t-t')}\hat{c}(t'), \tag{2.8}$$

where $t_0 < t$ is the initial time. The first term describes the free evolution of the bath mode. The second term is the dynamics due to the coupling to the system mode. Substituting Eq. (2.8) into Eq. (2.7), we find

$$\dot{\hat{c}} = \frac{i}{\hbar}[\hat{\mathcal{H}}_s, \hat{c}] - \int_{-\infty}^{\infty} d\omega \int_{t_0}^{t} dt'\, \kappa(\omega)^2 e^{-i\omega(t-t')}\hat{c}(t') - \int_{-\infty}^{\infty} d\omega\, \kappa(\omega) e^{-i\omega(t-t_0)}\hat{b}_0(\omega). \tag{2.9}$$

The first term describes the free evolution of the system. The second term is the system coupled to its earlier mode, which can be seen as a memory term. The third term is the system couple to the earlier mode of the bath. Now, we use the first Markov approximation. Here we assume κ is frequency independent, which is a good approximation in the frequency range we care about. We use γ to represent resonator-bath coupling rate.

$$\kappa(\omega) = \sqrt{\gamma/2\pi} \tag{2.10}$$

Now we define the input field as

$$\hat{b}_{in}(t) = -\frac{1}{\sqrt{2\pi}}\int_{-\infty}^{\infty} d\omega e^{-i\omega(t-t_0)} b_0(\omega). \tag{2.11}$$

Using the relation

$$\int_{-\infty}^{\infty} d\omega e^{-i\omega(t-t')} = 2\pi\delta(t-t'). \tag{2.12}$$

The commutation relation of the input field can be shown to satisfy

$$\begin{aligned}[\hat{b}_{in}(t), \hat{b}_{in}^{+}(t')] &= \frac{1}{2\pi}\int_{-\infty}^{\infty} d\omega_1 \int_{-\infty}^{\infty} d\omega_2 e^{-i\omega_1(t-t_0)} e^{i\omega_2(t-t_0)}[\hat{b}(\omega_1), \hat{b}^{+}(\omega_2)] \\ &= \delta(t-t').\end{aligned} \tag{2.13}$$

Employing the identity $\int_{t_0}^{t} c(t')\delta(t-t')dt' = \frac{1}{2}c(t)$, we can get

$$\begin{aligned}\int_{-\infty}^{\infty} d\omega \int_{t_0}^{t} dt' \kappa(\omega)^2 e^{-i\omega(t-t')}\hat{c}(t') &= \frac{\gamma}{2\pi}\int_{t_0}^{t} dt' \int_{-\infty}^{\infty} d\omega e^{-i\omega(t-t')}\hat{c}(t') \\ &= \gamma \int_{t_0}^{t} dt' \delta(t)\hat{c}(t') = \frac{\gamma}{2}\hat{c}(t).\end{aligned} \tag{2.14}$$

Putting all these pieces together, we get the Heisenberg equation for the field operator

$$\dot{\hat{c}} = \frac{i}{\hbar}[\hat{\mathcal{H}}_s, \hat{c}] - \frac{\gamma}{2}\hat{c} + \sqrt{\gamma}b_{in}(t). \tag{2.15}$$

This equation is called the quantum Langevin equation [20]. The first term describes the dynamics of the system. The second term represents the damping of the system. The last term represents the influence of an external mode on the system. We can also define the output field as

$$\hat{b}_{out}(t) = \frac{1}{\sqrt{2\pi}}\int_{-\infty}^{\infty} d\omega e^{-i\omega(t-t_1)}b_1(\omega), \tag{2.16}$$

where t_1 >t and $b_1(\omega) = b(\omega')|_{t=t1}$, and in analogy to the input mode, we get

$$\dot{\hat{c}} = \frac{i}{\hbar}[\hat{\mathcal{H}}_s, \hat{c}] + \frac{\gamma}{2}\hat{c} - \sqrt{\gamma}\hat{b}_{out}(t). \tag{2.17}$$

From Eqs. (2.11) & (2.17), we can get the boundary condition of the input-output field

$$\hat{b}_{in} + \hat{b}_{out} = \sqrt{\gamma}\hat{c}. \tag{2.18}$$

2.2. Input-output theory of an electrical resonator coupling with an acoustic resonator

For our system, the setup is an electrical resonator piezoelectrically coupled to an acoustic resonator. The Hamiltonian of the system is

$$\hat{\mathcal{H}}_s = \hbar\omega_a\hat{a}^+\hat{a} + \hbar\omega_c\hat{c}^+\hat{c} + \hbar g_{ea}(\hat{a}^+\hat{c} + \hat{a}\hat{c}^+), \tag{2.19}$$

where $\hat{a}$ and $\hat{a}^+$ are the annihilation and creation operators for the acoustic mode. $\hat{c}$ and $\hat{c}^+$ are the annihilation and creation operators for the electrical mode. g_{ea} is the coupling strength between the electrical mode and the acoustic mode. The first term describes the energy of the acoustic mode. The second term is the Hamiltonian of the electrical mode. The third term is the interaction between the two resonators. The time evolution of the electrical mode is

$$\dot{\hat{c}} = -i\omega_c - ig_{ea}\hat{a} - \frac{\kappa_{total}}{2}\hat{c} + \sqrt{\kappa_c}\hat{b}_{in}, \tag{2.20}$$

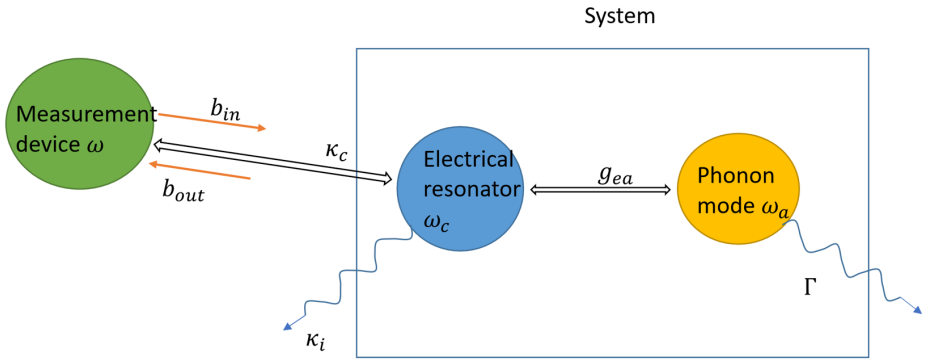

Figure 2.1.: Schematic diagram of our system. κ_c is the coupling rate between the measurement device and the electrical resonator, g_{ea} is the coupling rate between the electrical resonator and the acoustic resonator. κ_i and Γ are the decay rate of the photon in the electrical resonator and the phonon in the acoustic resonator respectively.

where $\kappa_{total} = \kappa_i + \kappa_c$. κ_c is the coupling rate of the electrical resonator to the measurement device and κ_i is the decay rate to other channels. From Eq. (2.11), The time evolution of the acoustic mode can be written as

$$\begin{aligned}\dot{\hat{a}} &= \frac{i}{\hbar}[\hat{\mathcal{H}}_s, a] - \frac{\Gamma}{2}\hat{a} \\ &= -i\omega_a\hat{a} - ig_{ea}\hat{c} - \frac{\Gamma}{2}\hat{a}.\end{aligned} \tag{2.21}$$

The driving frequency is ω. Therefore in equilibrium condition, we can assume $\hat{a}(t) = \widetilde{a}e^{-i\omega t}$, $\hat{c}(t) = \widetilde{c}e^{-i\omega t}$. And plugging these into Eq. (2.21)

$$-i\omega\widetilde{a} = -i\omega_a\widetilde{a} - ig_{ea}\widetilde{c} - \frac{\Gamma}{2}\widetilde{a}. \tag{2.22}$$

From this, we get the relation between $\widetilde{c}$ and $\widetilde{a}$:

$$\widetilde{a} = \frac{-ig_{ea}\widetilde{c}}{\frac{\Gamma}{2} - i(\omega - \omega_a)}. \tag{2.23}$$

Let us now substitute Eq. (2.23) into Eq. (2.20), and we can find

$$\widetilde{c} = \frac{\sqrt{\kappa_c}\widetilde{b}_{in}}{\frac{2g_{ea}^2}{\Gamma - 2i(\omega - \omega_a)} + \frac{\kappa_{total}}{2} - i(\omega - \omega_c)}. \tag{2.24}$$

The boundary condition can be written as

$$\widetilde{b}_{out} = -\widetilde{b}_{in} + \sqrt{\kappa_c}\widetilde{c}. \tag{2.25}$$

Finally, we can get the output field and define the reflection as

$$S_{11} = \frac{\widetilde{b}_{out}}{\widetilde{b}_{in}} = \frac{-\frac{2g_{ea}^2}{\Gamma - 2i(\omega-\omega_a)} + \frac{\kappa_c-\kappa_i}{2} + i(\omega-\omega_c)}{\frac{2g_{ea}^2}{\Gamma - 2i(\omega-\omega_a)} + \frac{\kappa_c+\kappa_i}{2} - i(\omega-\omega_c)}. \tag{2.26}$$

2.3. Reflection construction and hanger construction

There are several constructions of an experiment to measure the spectrum [21, 22]. Here, we emphasize two of them. One is reflection construction, which measures the reflection signal. Another one is referred to as hanger construction, in which an unbalanced tee replaces the circulator of the reflection circuit (see Figs 2.2, 2.4).

2.3.1. Reflection construction

We already derived the measured signal for the reflection construction in the last section using the input-output theory (Eq. (2.26)). We can also use methods from microwave engineering to derive it [23]. This will help us to understand the formula derived in section 2.3.2. We assume the total impedance in the red block in Fig 2.2 is Z_{total}. And the characteristic impedance of port 1 and port 2 is Z_0^{ref}. Based on the circuit analysis from Fig 2.2, S_{11}^{ref} is derived in Appendix A. The result is

$$S_{11}^{ref} = \frac{Z_{total} - Z_0^{ref}}{Z_{total} + Z_0^{ref}}. \tag{2.27}$$

Based on Eq. (2.26), the amplitude response and phase response of the spectrum can be seen in Fig 2.3. In the spectrum simulation, we assume the coupling factor of the electrical resonator and measurement device is $\kappa_c = 10\,\text{MHz}$, the internal loss rate of the electrical resonator is $\kappa_i = 50\,\text{kHz}$, frequency of the electrical resonator is $\omega_c = 6\,\text{GHz}$, frequency of the acoustic resonator is $\omega_a = 6.013\,\text{GHz}$, coupling rate between the electrical resonator and the acoustic resonator is $g_{ea} = 500\,\text{kHz}$, the decay rate of the acoustic mode is $\Gamma = 20\,\text{kHz}$. These values are chosen based on the previous articles' results and the simulation which will be explained in the next chapter [18, 21]. From the plot we can see that both, amplitude and phase response, show a wide peak around 6 GHz, corresponding to the electrical resonance. The thinner peak near 6.013 GHz is the resonance of the acoustic resonator. The width of the resonance of the electronic resonator is $\kappa_i + \kappa_c$, and the contrast ratio is $\frac{\kappa_i}{\kappa_i+\kappa_c}$, explaining the contrast of the peak is much smaller than 1.

2.3.2. Hanger construction

The advantages of the hanger construction are no requiring special circuits elements and support for many resonators to be multiplexed measured with the same input-output lines[21]. Fig 2.4 shows the circuit representation of the hanger measurement. It looks similar to the reflection measurement, except the signal outputs from port 2 directly

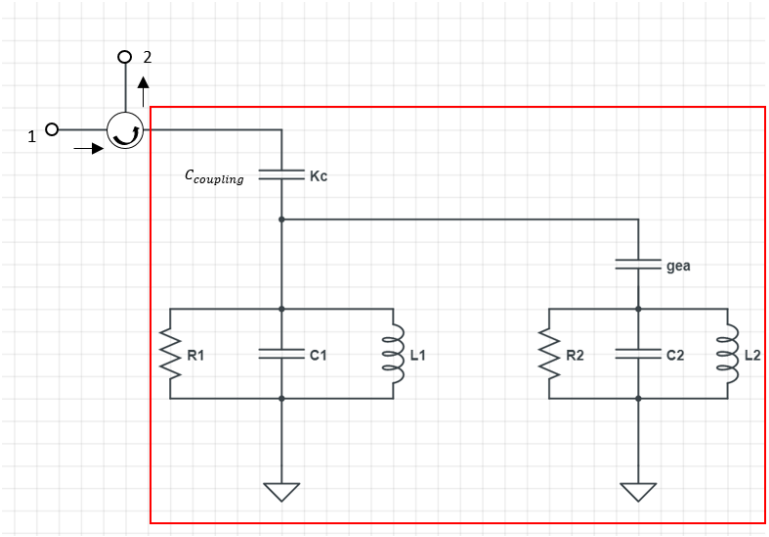

Figure 2.2.: Circuit representation of reflection measurement construction. Element R1, C1, and L1 represent electrical resonator. Element R2, C2, and L2 represent the acoustic resonator. The electrical resonator is capacitively coupled with the measurement device. The acoustic resonator is coupled with electrical resonator piezoelectrically, which also be represented with the electrical circuit for convenience. The input signal comes in from port 1. The reflected signal comes out from a circulator and to port 2.

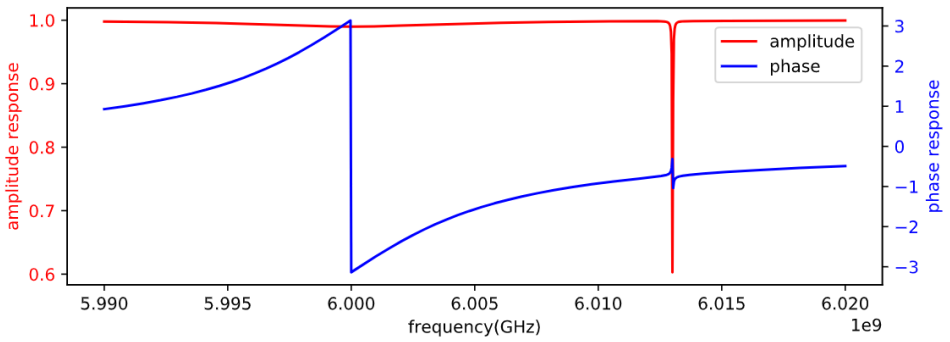

Figure 2.3.: Frequency response of S_{11}^{ref} . The blue curve represents phase response of S_{11}^{ref} spectrum. The red curve represents amplitude response of S_{11}^{ref} spectrum

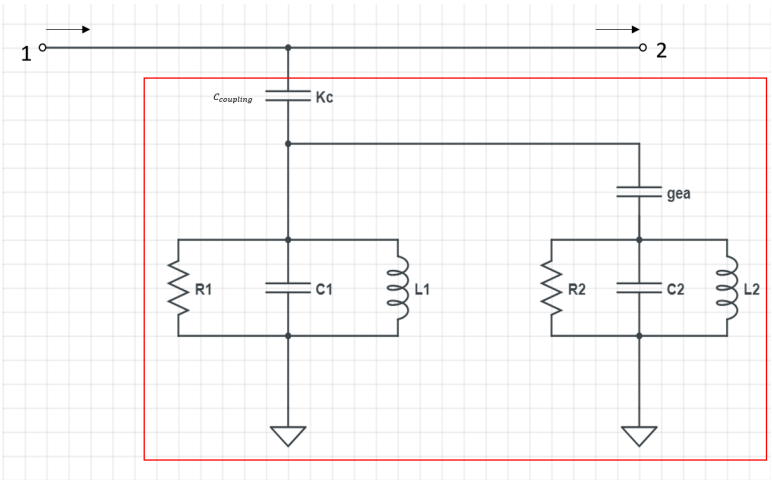

Figure 2.4.: Circuit representation of hanger measurement construction.

instead of reflecting back. We assume the total impedance in the red block in Fig 2.2 is Z_{total}, which similar to the reflection measurement. The characteristic impedance of port 1 and port 2 is Z_0^{hanger}. From analyzing the scattering matrix of this circuit (Appendix B), the transmission signal S_{21}^{hanger} can be written as

$$S_{21}^{hanger} = \frac{Z_{total}}{Z_{total} + \frac{Z_0^{hanger}}{2}}. \tag{2.28}$$

If we set $Z_0^{hanger} = 2Z_0^{ref}$, then we can find the simple relation between S_{21}^{hanger} and S_{11}^{ref}

$$S_{21}^{hanger} = \frac{1}{2}(1 + S_{11}^{ref}) = \frac{1}{2}(1 + \frac{-\frac{2g_{ea}^2}{\Gamma - 2i(\omega-\omega_a)} + \frac{\kappa_c - \kappa_i}{2} + i(\omega - \omega_c)}{\frac{2g_{ea}^2}{\Gamma - 2i(\omega-\omega_a)} + \frac{\kappa_c + \kappa_i}{2} - i(\omega - \omega_c)}). \tag{2.29}$$

We can understand this equation in the following way: In hanger construction, an unbalanced T shape replaces the circulator in reflection construction. From the load impedance side (red block in Fig 2.4), the effective impedance of the wire is a parallel connection of port 1 and port 2 which is equal to half Z_0^{hanger}. In this way, part of the incident energy does not dissipate in the load impedance, and part of the reflected energy from the load impedance goes to port 1.

Fig 2.5 is the phase and the amplitude response of the hanger construction with the same parameters as in Fig 2.3. Comparing the amplitude response of these two constructions, we can find the contrast of the electrical resonance is deeper in the hanger construction in the regime that $\kappa_c \gg \kappa_i$.

In the real experiment, because of the convenience to measure multiple resonators at the same time, we decided to use the hanger construction. We will measure the $S_{21}^{hanger}(\omega)$

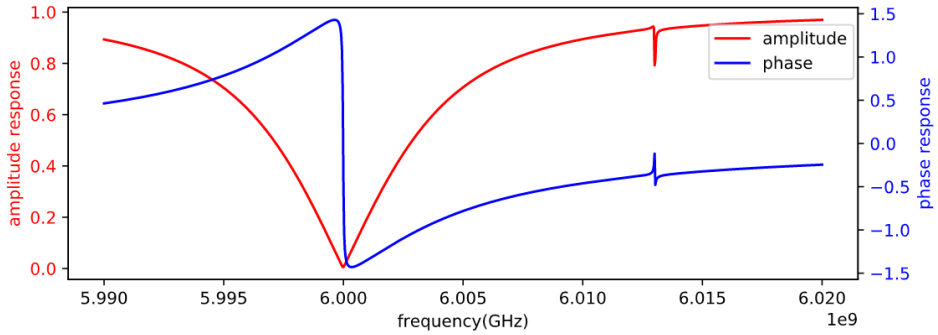

Figure 2.5.: Frequency response of S_{21}^{hanger}. The blue curve represents phase response of S_{21}^{hanger} spectrum. The red curve represents amplitude response of S_{21}^{hanger} spectrum

and using Eq. (2.29) to fit g_{ea} and Γ, which we expect to measure. This is the logic of this thesis.

Chapter 3

Simulation and device design

In last chapter, we have shown the derived formula of the spectrum we expect to measure. And we will get the values we want by fitting with this formula. Therefore we need to choose the experiment parameters for easier fitting. In this chapter, we first introduce the flip-chip construction in section 3.1. Followed by the introduction of the electrical resonator and high overtone bulk acoustic resonator in section 3.2 and 3.3, and finally we show how we choose the design parameters of our experiment in the rest of this chapter.

3.1. Flip-chip construction

We use flip-chip construction to implement the experiment. The electrical resonator and acoustic resonator are on two different chips which are bonded together. The distance between two chips is designed to be 4 μm. This geometry allows us to design, optimize, and fabricate the electrical resonator and acoustic resonator separately to reduce the acoustic resonator decay while enhancing the selectivity of the coupling to a single mode [18]. There is an antenna connected to the electrical resonator. The antenna overlaps with the piezo layer on the other chip, which induces coupling between the electrical resonator and the acoustic resonator. The thickness of the piezoelectric material is about 1 μm.

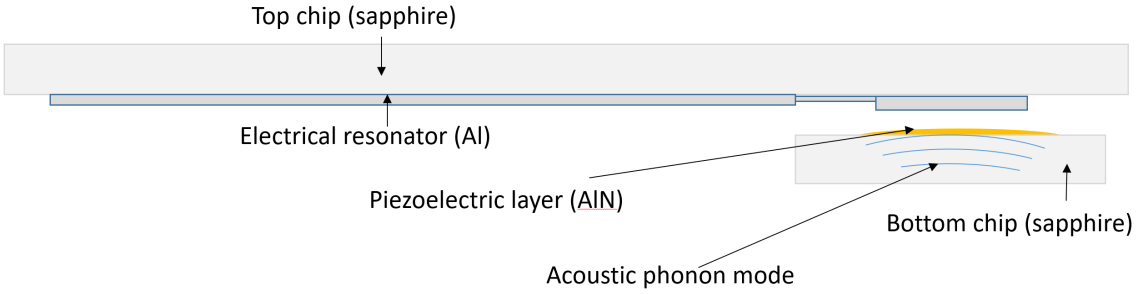

Figure 3.1.: Schematic of flip chip construction.

Fig 3.1 is the schematic of the flip-chip construction. The top chip is made of sapphire, which has excellent electrical insulating properties and thermal conductivity. The electrical resonator is printed onto the top chip and is made of aluminum. We choose aluminum because it becomes superconducting at low temperature, reducing the internal loss. Beneath the antenna of the electrical resonator, the bottom chip made of sapphire

is bonded in place. The cross section of the bottom chip resonator is covered with a dome-shaped aluminum nitride (AlN) layer, which is aligned with the electronic antenna on the top chip during the bonding process. The bottom chip itself functions as a high overtone bulk acoustic resonator (HBAR), where modes are confined to the cross section defined by the AlN layer. The thickness of the chip depends on the wafer chosen, which is normally 420 μm.

3.2. Electrical resonator

We use the electrical resonator to measure the properties of the acoustic wave. The electrical resonator we use is a half-wavelength resonator, which indicates the length of the resonator is integral times of the half-wavelength. The resonator is put inside a cavity along the longitude direction. There are two holes on the cavity to let a copper pin get through the cavity, where the input signal transits through. The electrical resonator couples with the pin and the cavity capacitively. The cavity is the ground plane. We want to couple the superconducting qubit to acoustic phonons in the future. Therefore, we are more curious about the properties of the phonons that have frequencies in the range of 5 to 7 GHz, the same as the typical operating range of our transmon qubits [24]. So, we also need to design the resonator in this range, which corresponds to a total length of resonator pad and antenna lead roughly 12 mm to 18 mm.

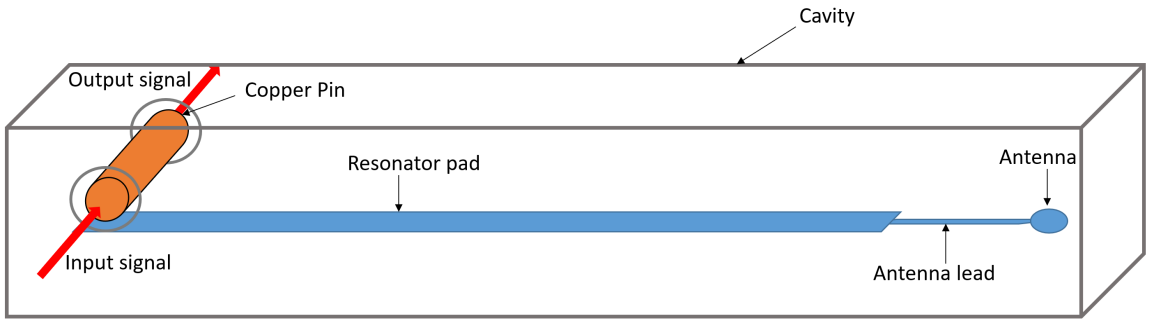

Figure 3.2.: Schematic of the electrical resonator. There are three parts of the electrical resonator. The left part is the resonator pad, and the right part is the antenna. The resonator pad and the antenna are connected by a thin antenna lead. The electrical resonator is put inside a cavity and capacitively coupling to the cavity and the pin.

3.3. Acoustic resonator

3.3.1. Quantization of phonon mode

Analogous to electromagnetic modes, suppose the phonon mode has the form of [25–27]

$$\vec{u}(\vec{r},t) = u_0 e^{-i\omega t}\vec{f}(\vec{r}) + c.c. = u_0(t)\vec{f}(\vec{r}) + c.c.\,, \tag{3.1}$$

where $\vec{u}(\vec{r},t)$ represents displacement at point $\vec{r}$ and time t, $\vec{f}(\vec{r})$ is the spatial dependence and polarization of the displacement which is normalized to

$$\int \left|\vec{f}(\vec{r})\right|^2 dV = 1. \tag{3.2}$$

$\vec{u}(\vec{r},t)$ should fulfill Newton's second law:

$$\rho\frac{\partial^2\vec{u}}{\partial t^2} = \nabla\overleftrightarrow{T}(\vec{x}), \tag{3.3}$$

where T is the stress tensor. Expressing the stress tensor by the displacement, we get

$$\rho\frac{\partial^2\vec{u_i}}{\partial t^2} = \sum_{jlm} c_{ijlm}\frac{\partial^2 u_l}{\partial x_j \partial x_m}, \tag{3.4}$$

where c_{ijlm} is the stiffness tensor. i,j,l,m change from 1 to 3 and represent the three canonical directions. The Hamiltonian of the system is

$$\begin{aligned} H &= T + V \\ &= \int (\frac{\rho}{2}\sum_i \left|\frac{\partial u_i}{\partial t}\right|^2 + \frac{1}{2}\sum_{ijlm} c_{ijlm}\frac{\partial u_i}{\partial x_j}\frac{\partial u_l}{\partial x_m})dV. \end{aligned} \tag{3.5}$$

Revisiting the potential energy term:

$$\begin{aligned} V &= \int \frac{1}{2}\sum_{ijlm} c_{ijlm}\frac{\partial u_i}{\partial x_j}\frac{\partial u_l}{\partial x_m}dV \\ &= \frac{1}{2}\int \sum_{ijlm}[\frac{\partial}{\partial x_j}(u_i\frac{\partial u_l}{\partial x_m}) - u_i\frac{\partial^2 u_l}{\partial x_j \partial x_m}]dV \\ &= \frac{1}{2}\int dS\hat{n}\cdot(\sum_{ijlm} u_j\frac{\partial u_l}{\partial x_m}) - \frac{1}{2}\int dV\sum_j u_j\sum_{jlm} c_{ijlm}\frac{\partial^2 u_l}{\partial x_j\partial x_m} \\ &= \frac{1}{2}\int dS\hat{n}\cdot\sum_j u_i T_{ij} - \frac{1}{2}\int_d V\sum_j u_j\rho\frac{\partial^2\vec{u_i}}{\partial t^2} \\ &= \frac{1}{2}\int dS\hat{n}\cdot\sum_j u_i T_{ij} + \frac{1}{2}\int_d V\sum_j \omega^2\rho u_j^2, \end{aligned} \tag{3.6}$$

where the left term is the energy flow leaves from the boundary surface of the volume, which can be assumed to be 0 in our model. The derivation of the right term uses Eq. (3.4). Inserting this result in Eqs. (3.6) & (3.5), we can get

$$H = \frac{1}{2}\rho\omega^2|iu_0(t) - iu^*(t)|^2 \int \left|\vec{f}(\vec{r})\right|^2 dV + \frac{1}{2}\omega^2\rho|u_0(t) + u_0^*(t)|^2 \int \left|\vec{f}(\vec{r})\right|^2 dV. \quad (3.7)$$

If we define the conjugate variables:

$$\hat{p} = -\omega\rho(u_0(t) + u_0^*(t))), \quad (3.8)$$

$$\hat{q} = -(iu_0(t) - iu_0^*(t)). \quad (3.9)$$

We obtain the harmonic oscillator Hamiltonian:

$$H = \frac{\hat{p}^2}{2\rho} + \frac{1}{2}m\omega^2\hat{q}^2. \quad (3.10)$$

Then we use creation and annihilation operators to replace $\hat{p}$ and $\hat{q}$

$$\hat{p} = -i\sqrt{\frac{\rho\hbar\omega}{2}}(\hat{a} - \hat{a}^\dagger), \quad (3.11)$$

$$\hat{q} = \sqrt{\frac{\hbar}{2\rho\omega}}(\hat{a} + \hat{a}^\dagger). \quad (3.12)$$

And we can get

$$H = \hbar\omega\hat{a}^\dagger\hat{a} + const. \quad (3.13)$$

Therefore, the quantum displacement operator can be written as

$$\hat{u}(\hat{r}, t) = \sqrt{\frac{\hbar}{2\rho\omega}}(i\hat{a}(t) - i\hat{a}^\dagger(t)). \quad (3.14)$$

Finally, we have found the expression for the quantized phonon mode.

3.3.2. Shape of phonon mode

Due to our acoustic cavity design, in analogy to a Fabry-Perot optical cavity, the acoustic phonon modes in our experiment have a Hermite-Gaussian mode profile. For simplicity, we select the cavity axis as the polarization direction, so we only have to consider the strain field along the z-axis. For simplicity, we can consider it has the form

$$S_{33} = \frac{\partial u_3}{\partial x_3} = s_{n,m}(x, y)cos(q \cdot z). \quad (3.15)$$

Here, S_{33} is the strain field along the z-axis. $s_{n,m}$ represents the transverse profile of the strain field, where n and m represent the transverse mode numbers, and q is the wave

vector of the phonon mode. For Hermite-Gaussian modes, $s_{n,m}$ can be expressed as

$$s_{nm}(x,y) = \frac{S_0}{r_0}\sqrt{\frac{n!m!}{2^n 2^m}} e^{\left(\frac{(x-x_0)^2+(y-y_0)^2}{2r_0^2}\right)} H_n\left(\frac{x_x 0}{r_0}\right) H_m\left(\frac{y_y 0}{r_0}\right), \tag{3.16}$$

where H is a Hermite polynomial equation, and S_0 is a normalization factor. For different n,m values, $s_{n,m}$ is orthogonal to each other.

$$S_0 = \sqrt{\frac{8\hbar\omega}{c_{33}l}} \tag{3.17}$$

From Fig 3.3, we can find that the 00 Hermite-Gaussian mode is in a two-dimensional Gaussian shape and have the same phase on the transverse plane. We want to couple the acoustic resonator with the 00 mode. However, there always exist several transverse modes for each longitudinal phonon mode in the acoustic resonator. In order to selectively couple to a dedicated transverse mode, we need to design the antenna shape according to 00 mode. Therefore we need to design the antenna shape to emit Gaussian transverse electric field or as close as possible to avoid coupling to other modes.

3.4. Coupling between the electrical resonator and the measurement device

We want to get the values of g_{ea} and Γ by using Eq. (2.29) to fit $S_{21}^{hanger}(\omega)$. In order to have higher fitting precision, we need to choose appropriate coupling strength between the electrical resonator and the measurement device. The way we choose it is by generating simulated spectra based on Eq. (2.29) with different κ_c and fitting the simulated spectra and comparing fitting errors of g_{ea} and Γ. For each value of κ_c, we generate 1000 simulated spectra with different random noise. The random noise is of 0.25% level. Then we fit each spectrum and calculate the standard deviation of fitted g_{eq} and κ_i. Remaining parameters in simulated spectra are set as $\kappa_i = 50\,\text{kHz}$, $\omega_c = 5.994\,\text{GHz}$, $\omega_a = 6\,\text{GHz}$, $\Gamma = 20\,\text{kHz}$, $g_{ea} = 400\,\text{kHz}$. These values are chosen based on previous paper and simulation experience [18, 21].

We use two different approaches to fit the result. One is using the absolute value of Eq. (2.29) to fit for amplitude, another one is using the complex formula Eq. (2.29) to fit directly. The result is shown in Figs 3.4 & 3.5. Both approaches are fitted with the least square method [28]. We can see from the figure that the complex fitting has a better result compared to the amplitude fitting. This is expected since the complex function contains an additional degree of freedom. The figure also shows, for κ_c bigger than 5 MHz, the fitting error for g_{ea} and Γ are suppressed. This suppression can be understood as, we measure the acoustic resonator mediated by the electrical resonator, a stronger coupling between the electrical resonator and the measurement cavity also improves the signature of the acoustic resonator in the spectrum. From these results, we aim for a value of κ_c above 5 MHz. In the simulation of our setup, the highest κ_c we

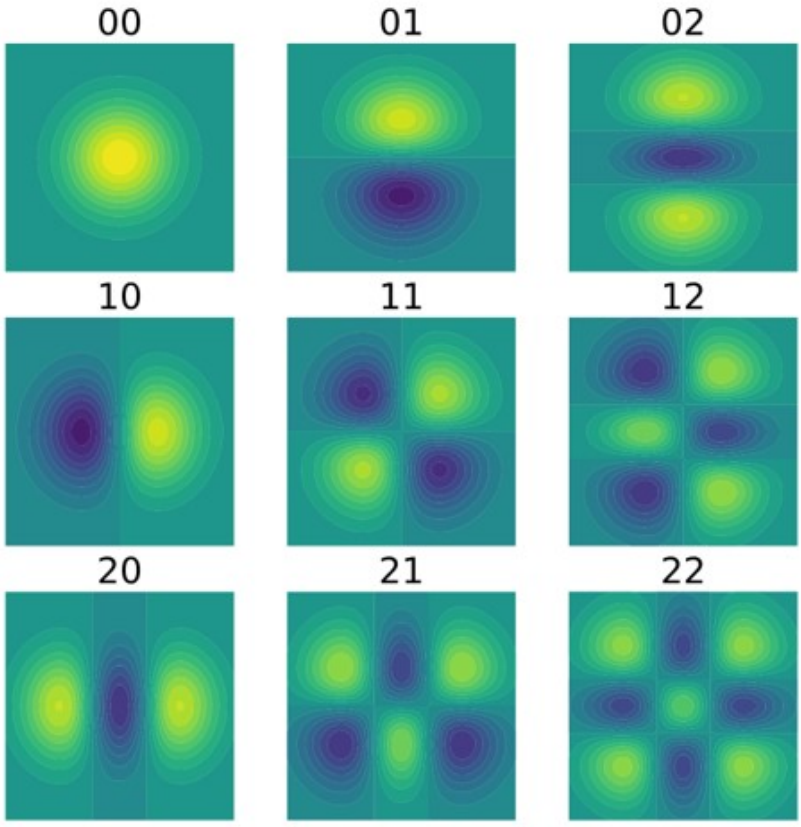

Figure 3.3.: Shape of different Hermite-Gaussian transverse modes.

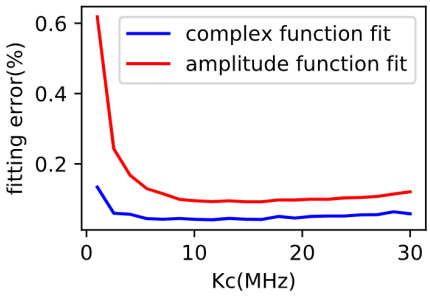

Figure 3.4.: Fitting result of g_{ea} based on artificial data

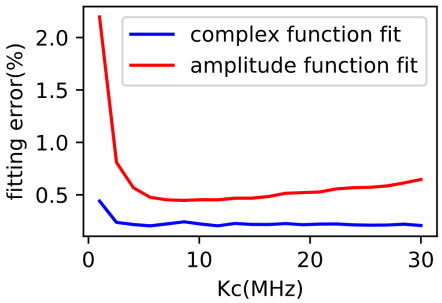

Figure 3.5.: Fitting result of Γ based on artificial data

could get is about $50\,MHz$. So there is no upper bound for appropriate κ_c in our system.

The next question we need to think about is what design parameters determine the κ_c value. Intuitively, the coupling factor should depend on the relative distance from the electrical resonator to the pin connecting the input and the output port of the cavity. It should also be related to the geometry of the resonator. We make a simple model in ANSYS to simulate the experiment as shown in Fig 3.6.

The sketch of the relative position of pin and oscillator is shown in Fig 3.7. First, we fix the relative z distance and the width of the resonator, and sweep the relative y distance. The result is shown in Fig 3.8. When the relative y distance is 1 mm, κ_c is maximised. When we sweep the relative distance in z-direction shown in Fig 3.9, κ_c is bigger if the relative distance is smaller.

Fixing the relative position of pin and resonator and changing the width of the oscillator, we observe increasing κ_c for increasing resonator width, which is shown in Fig 3.10. This can be understood as, the resonator is capacitively coupling to the pin and cavity box, the bigger the size, the higher the capacitance, and the stronger the coupling.

To summarize, we can tune κ_c by changing the relative position of pin and resonator, or by changing the geometry of the resonator pad. κ_c bigger than 5 MHz can be achieved, in which regime we hope to be able to precisely fit our data.

3.5. Coupling between the electrical resonator and the acoustic resonator

In the last section, we have discussed the coupling between the electrical resonator and the measurement device. In this section, we will discuss the coupling between the electrical resonator and the acoustic resonator. In the future experiment, we want to achieve fast operations between the qubit and acoustic modes, so we need to find the appropriate design for large coupling between these two. Therefore, in our characterization experiment, we also want to achieve faster coupling between the electrical resonator and the acoustic mode.

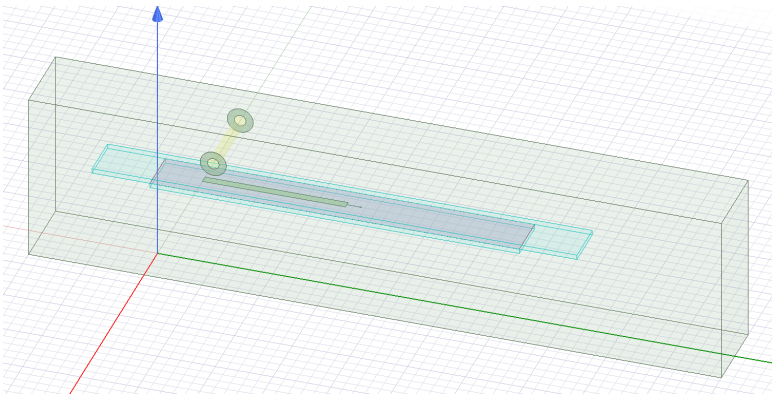

Figure 3.6.: The sketch of the simple model in ANSYS. We use a cuboid as the cavity in the simulation for simplicity. It has similar dimensions to the actual cavity. The two transparent blue chips are sapphire. The pink part is the piezoelectric layer. The green stripline is the electrical resonator, which is set as a perfect conductor. The light yellow tube is the measurement pin. The two green rings are set as 50 Ω as the boundary condition. The cavity is set as a perfect conductor as the boundary condition.

Figure 3.7.: Sketch of the relative position of pin and electrical oscillator

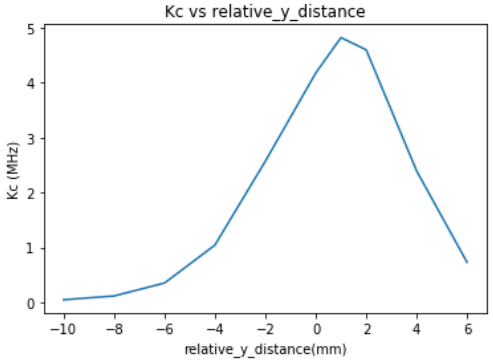

Figure 3.8.: κ_c changes with relative y distance

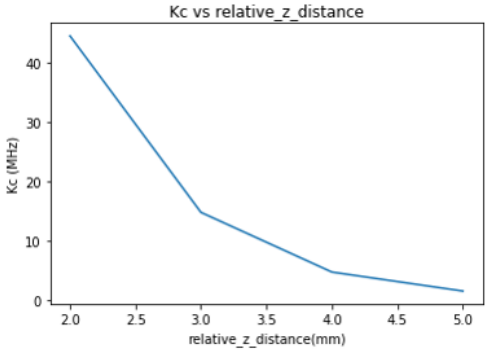

Figure 3.9.: κ_c changes with relative z distance

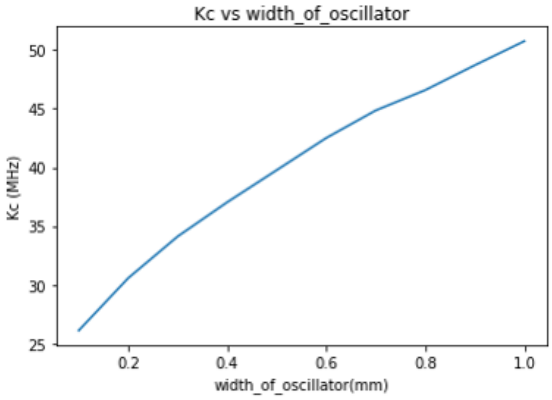

Figure 3.10.: κ_c changes with width of oscillator

The coupling between the electrical resonator and the acoustic resonator is mediated by the piezoelectric effect. The electric field generated from the antenna causes a strain in the piezoelectric crystal that excites the phonon mode at the electric field frequency. For simplicity, we only consider the electric field perpendicular to the chip, which is z-direction in our setting. The coupling strength between these two resonators is [17]

$$g_{ea} = \int_V \sigma(x, y, z) S(x, y, z) dV, \tag{3.18}$$

where $\sigma(x, y, z) = c_{33} d_{33} E(x, y, z)$ is the stress field in the piezoelectric layer. c_{33} and d_{33} are the stiffness tensor and the piezoelectric tensor along the z-direction respectively. $E(x, y, z)$ is the electric field along the z-direction. $S(x, y, z)$ is the strain field of the phonon mode. Integration volume V is the whole volume of the piezoelectric layer. In our simulation, g_{ea} normally ranges from 300 kHz to 700 kHz depending on the shape of the antenna and the size of the mode.

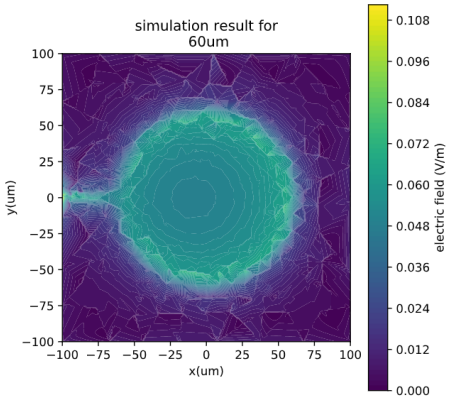

Figure 3.11.: electric field generated by an 60 μm radius antenna

In order to calculate the coupling factor between the two resonators, we also need to know the electric field generated by the antenna. The electrical field data can be exported from ANSYS and analyzed. The electric field generated by a circular antenna does not produce a Gaussian shape. We can see from Fig 3.11, the field at the edge is larger than the field in the center, which can cause the coupling to other higher order transverse Hermite–Gaussian modes. Therefore, we need to find an appropriate radius for the antenna to achieve higher coupling with the 00 mode and smaller coupling to other modes. However, these two requirements mostly contradict each other, so we need to have a more specific criterion to design the antenna.

3.6. Antenna design

3.6.1. Criterion for design of antenna

As we mentioned in the last section, we need a criterion to design the antenna to balance higher coupling to the 00 mode and smaller coupling to other orthogonal modes. One criterion that can be used is the fidelity of the swap gate. For this, we prepare the qubit initially in the excited state and the phonon mode in the zero Fock state. We let the qubit frequency be the same as 00 mode frequency of the resonator, and simulate the population of a single phonon excitation due to a swap operation. Here we assume, if the electrical resonator and superconducting qubit have the same antenna, the shape of the electric field generated by the antenna is the same in both resonator and qubit case. Thus, for simplicity, we can use the electrical resonator to simulate. We can use parameters in previous research in our simulation, where T_1 of qubit is 7 μs, T_1 of phonon mode is 64 μs, and T_2 of phonon mode is 40 μs [18].

Figs 3.12a & 3.12b show the change of the fidelity of the swap operation for increasing coupling strength to the 01 mode and 02 mode separately. For these two plots, we use a coupling strength to the 00 mode of 600 kHz. We can deduce the decay of the system will cause infidelity of about 3.6%, which is shown at the 0 coupling point. Comparing these

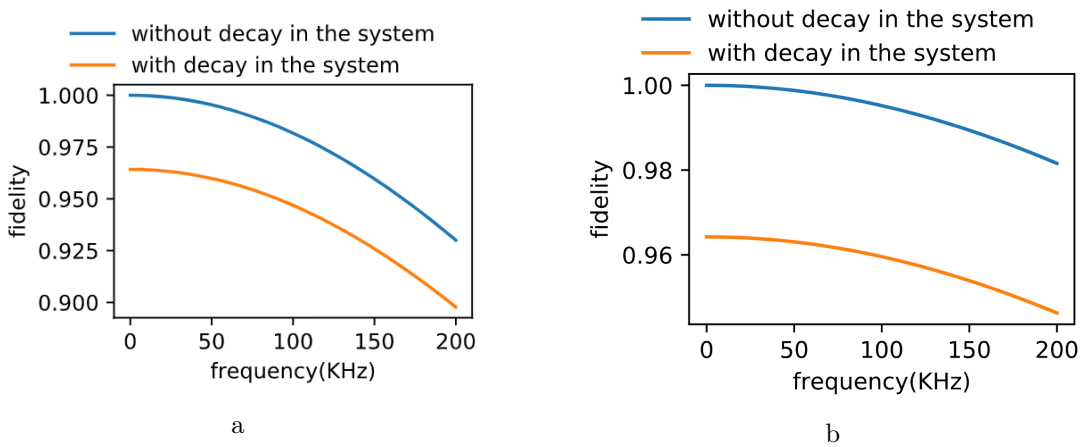

Figure 3.12.: (a) swap gate fidelity changing with coupling factor to 01 mode. (b) swap gate fidelity changing with coupling factor to 02 mode. Coupling factors to other mode are set 0. We plot the fidelity for both with and without considering the decay in the system.

two figures, we find that the coupling factor to the 01 mode has a much stronger effect because it is less detuned from the qubit frequency. Furthermore, the effect of detuned coupling to the further higher-order transverse modes can be neglected. If we can keep the 01 mode coupling factor below 25 kHz, and 02 mode coupling factor under 50 kHz, the effect of coupling to higher transverse mode is not the dominant term of the infidelity for the swap operation.

As we mentioned before, if we use the simple circle shape of the antenna, the field generated is lager on the edge and smaller in the center, which is a different shape compared with 00 Hermite–Gaussian mode, and can cause the coupling to other modes. From here, we can try two things, one is we simulate different radii of the antenna circle and use this swap gate fidelity criterion to search for the appropriate radius. Second, we can try several different shapes of the antenna in the simulation.

3.6.2. Different radius for circle antenna

We assume the 00 mode we want to couple has a radius of 47 μm. This radius is chosen based on the previous fabrication result. We sweep the radius of the antenna in ANSYS and export the simulation field data. The coupling factors between the electrical resonator and the six different transverse phonon modes with the lowest energy are calculated. Furthermore, based on the coupling factor, the fidelity of the swap gate was calculated. The higher order transverse modes have much bigger detuning and much less effect on fidelity. Therefore this is a reasonable simplification.

From Fig 3.13, we can see the coupling rate to 00 mode gets higher for larger radii up to 68 μm. Also, the coupling rate to 10 mode gets smaller in this range. However, the coupling rate to 20 mode gets lager very fast with increasing radius. Therefore, at the

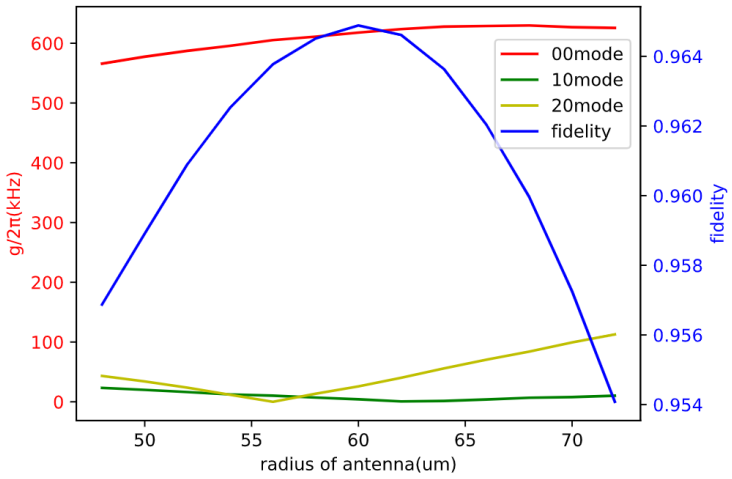

Figure 3.13.: Simulation result of changing the radius of antenna circle. The red curve is the coupling factor between the electrical resonator and the acoustic resonator 00 mode. The green curve is the coupling factor with the 10 mode. The yellow curve is the coupling factor with the 20 mode. The blue curve is the fidelity calculated based on the coupling factor of the simulation result

radius of 60 μm, the fidelity of the swap gate gets a maximum of 96.49%, which is the compensation point of the two effects mentioned above.

3.6.3. Different shape of antenna

Besides using a circular shaped antenna, we can also try different antenna shapes based on the swap gate fidelity criteria. Because we know at the edge of the antenna, there is a larger electrical field, one intuitive approach is increasing the perimeter length of the antenna. Thus we tried simulating a polygon shape antenna.

From Fig 3.14 we can see, the electric field generated by a polygon shape antenna is "flower" shaped. The "petal" of the flower has length 60um and the top part of the petal's width is 14 μm.

shape	00mode	01mode	02mode	10mode	11mode	20mode	fidelity
circle(kHz)	617	4.1	25.7	0.37	0.4	2.7	96.49%
polygon(kHz)	615	5.2	26.5	0.02	0.04	2.07	96.47%

Table 3.1.: Table of coupling strength to different mode for circle and polygon shape antenna.

Table.3.1 shows the coupling strength to different phonon modes and also the fidelity of

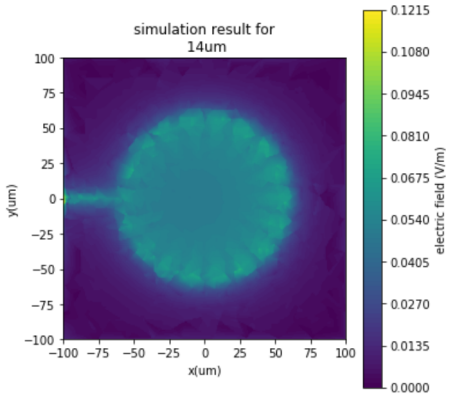

Figure 3.14.: Electrical field generated by polygon shape antenna.

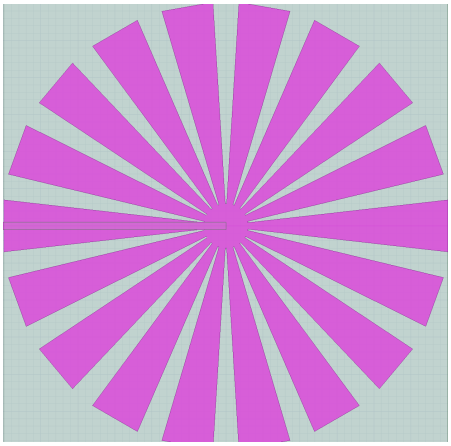

Figure 3.15.: Shape of the polygon antenna.

the swap gate for both antenna shapes, circular and polygon. From the simulation result, they show roughly the same result for coupling strength to each mode and final fidelity. We also calculate the fidelity of the swap gate without considering the decay in the system, and we can get the infidelity caused by the coupling to higher mode is 0.038% for the circle shape antenna, and 0.041% for the polygon shape antenna. The small infidelity caused by coupling to higher-order transverse modes also means the infidelity is dominated by the decay of the qubit and phonon in our current experimental conditions.

Because of the finite accuracy of the simulation, we can't make a conclusion towards which shape of the antenna is better. So both of the shapes are worthy to be characterized in the real experiment.

Chapter 4

Fabrication method and measurement setup

In last chapter, we introduce the design of each part of the system. In this chapter, we will first introduce the fabrication of the electrical resonator and acoustic resonator. Then we show the bonding of the two chips and the effect can be caused by the mismatch in the bonding procedure. At the end, we show the multiplexing setup and dilution fridge setup for the experiment.

4.1. Fabrication of electrical resonator

We use a conventional optical lithography technique to fabricate the electrical resonator [29, 30]. The resonator is fabricated on a sapphire wafer. The procedure is shown in Fig 4.1. After the cleaning of the wafer, the bilayer of the optical resist is spun on the wafer and baked. We use MA6 by Karl Suss to expose the optical resist with UV light, and then we evaporate aluminum in a Plassys shadow evaporator. In the end, we wash away the resist and dice the wafer into individual chips.

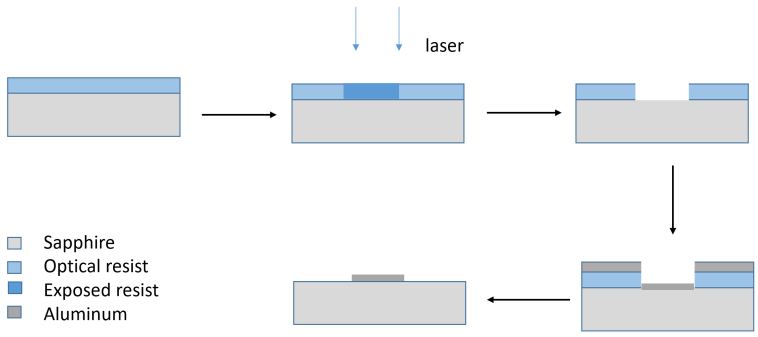

Figure 4.1.: Cross section of each part of the procedure for the fabrication of the electrical resonator.

Figure 4.2.: Cross section of each part of the procedure for fabrication of the acoustic resonator.

4.2. Fabrication of acoustic resonator

To fabricate the acoustic resonator, we use a sapphire wafer with a layer of c-axis oriented AlN with a width of 1 μm grown on one side [18]. First we pattern disks of photoresist on the wafer. Then the wafer is attached to a heated chuck and put inversely above a heated beaker of solvent. After 2-3 hours, the resist will absorb the solvent and turn into a hemisphere because of the surface tension. After that, we bake the wafer to remove the residual solvent and harden the resist. Then we use an anisotropic etching process (ICP-RIE) in an Oxford ICP etcher to etch the wafer and finally form a curved surface on the AlN layer, which works analogously to a mirror in an optical cavity [31].

4.3. Bonding of the chips

After fabrication of the electrical resonator chip and acoustic resonator chip, we need to bond them together. We pattern special align marks for aligning two chips on the horizontal direction, such that the electric field generated by the antenna can match the position of the acoustic mode. For the vertical direction, we make several spacers and set them on the surface of the acoustic resonator chip to guarantee the distance between two chips.

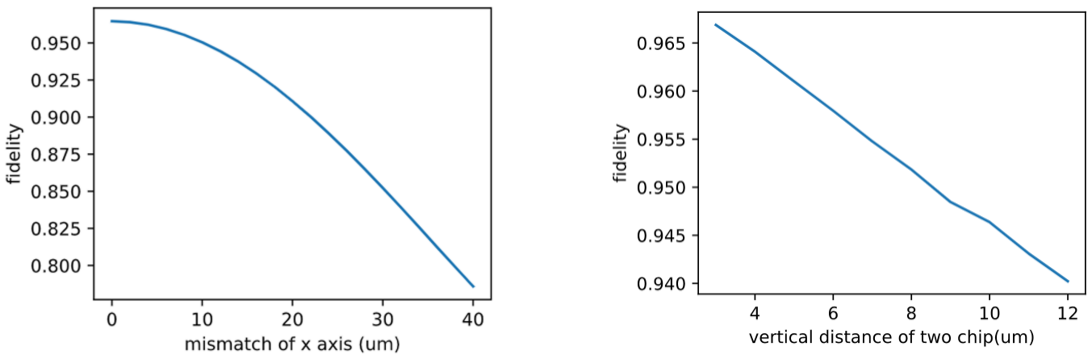

a b

Figure 4.3.: (a) How the mismatch along x axis affect the fidelity of swap gate. (b) How the vertical distance affect the fidelity of swap gate.

Figs 4.3a & 4.3b show how the fidelity of the swap changes with the mismatch along the x-axis (horizontal direction) and the z distance between two chips (vertical direction). The decrease of the fidelity is mainly caused by the decreasing coupling strength to the phonon's 00 mode which causes longer operation time and more decay of the qubit. From the figure, we can tell that if the mismatch in the horizontal direction is smaller than $5\,\mu$m, the effect of the mismatch can be ignored. As for vertical direction, it will be better if we can have a closer distance between two chips.

4.4. Multiplexing setup

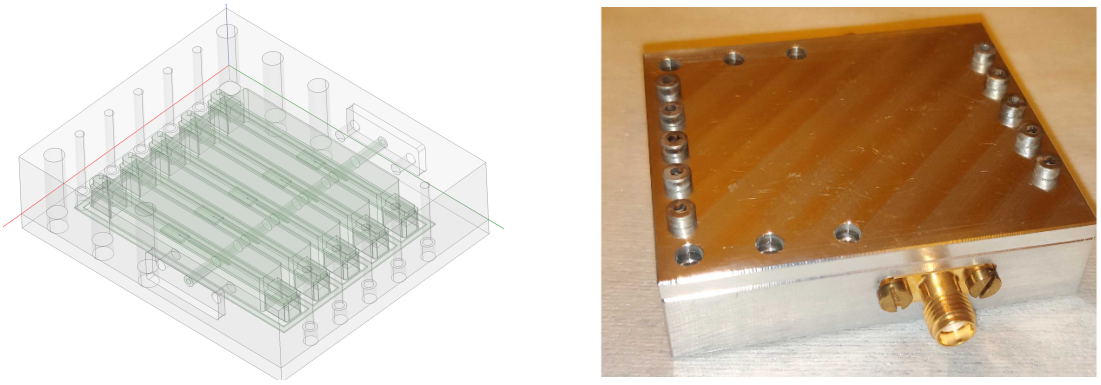

a b

Figure 4.4.: (a) Schematic of multiplexing setup (b) Assembled cavity box

We design a multiplexing setup to test several bonding chips within one experiment. There are five cavities in one cavity box, and we can put one chip into each cavity. There is a copper wire assembled in the cavity box as the measurement device pin. We use indium wire to fix the chips in the cavity and seal the cavity.

From the simulation result, the electric field generated by the antenna doesn't change a lot in this multiplex setup compared with the normal single cavity box. The coupling between the pin and the electrical resonator is also on the same scale and can be tuned by changing the relative position of the chip and the pin. As long as the electric resonator is designed carefully, and they are sufficiently frequency separated, we can assume the cross-talk between resonators can be neglected.

4.5. Dilution fridge setup

In the real experiment, we assemble the cavity and thermally connect it to the base temperature flange of a dilution refrigerator. At 1.2K, aluminum turns into a superconductor and has low energy loss [32]. Because the setup of the dilution fridge is designed for superconducting qubit experiments, it can be cooled down to 10mK. A vector network analyzer (VNA) is used to measure the spectrum. As shown in Fig 4.5, Port 1 of the

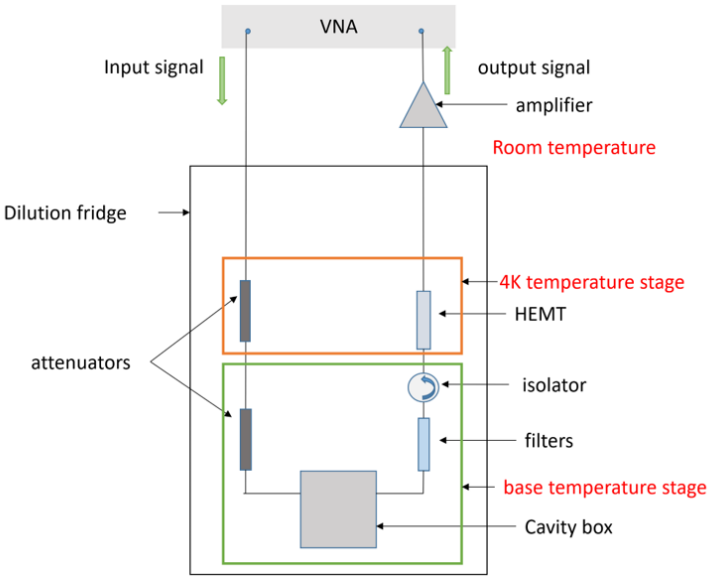

Figure 4.5.: Schematic of the cryogenic measurement setup. There are more stages in the fridge. But for simplicity, they are not drawn.

VNA is connected to the input port of the fridge, Port 2 of the VNA is connected to the output of the fridge. Several attenuators on different stages of the fridge are used to decrease the noise of the input channel [33]. After attenuation the input channel connects to the cavity. At the output channel, the output signal first passes filters and an isolator, to avoid signal reflection back into the cavity and suppress the noise traveling to the sample. There is a high electron mobility transistor (HEMT) on the 4K stage to amplify the output signal with low noise. Outside the fridge, the output signal is amplified again.

Chapter 5

Experimental results

5.1. Measurement of bare electrical resonators

Number of the chip	1	2	3	4	5
Length of the resonator pad(mm)	12	9	12	9	11
Length of the antenna lead (mm)	4	5	2	4	2
Antenna shape	circle	polygon	circle	polygon	circle
Simulated bare electrical resonator frequency(GHz)	5.869	6.228	6.625	6.861	7.050

Table 5.1.: Parameter of designed chips

In this project, we measure the bare electrical resonators in the multiplexing setup as a first step. For the next step, we would measure chips with acoustic resonators. But it's still work in progress and outside the scope of the thesis. The parameters of each chip are shown in Table.5.1. The chips are measured in a dilution fridge at 7 mK. We calibrated the phase response in VNA to compensate for the length effect of the cable. Besides, we use an external amplifier on the output signal to improve the signal to noise ratio.

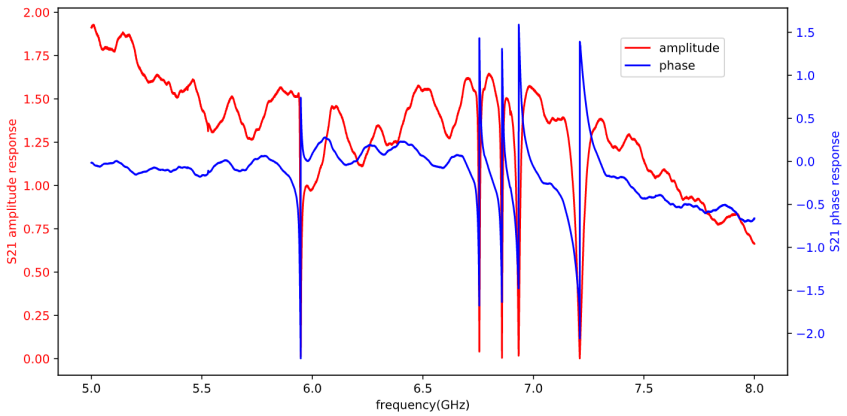

Figure 5.1.: Frequency response of S_{21} transmission. The red curve shows amplitude response. The blue curve shows phase response.

Fig 5.1 shows the frequency response of S_{21} transmission spectrum. We can see five peaks in both amplitude and phase spectrum. Due to the calibrated phase response, the phase spectrum doesn't show oscillation. The amplitude spectrum looks noisy because of the frequency response of the cables and amplifier in the setup. Therefore, we only fit normalized data close to each peak.

Because there is no acoustic resonator in the system, we can just write our fitting formula from Eq. (2.29), and assume the g_{ea} inside is 0. The fitting equation becomes

$$S_{21}(\omega) = Ae^{i\psi}(1 + e^{i\phi}\frac{-\kappa_c + \kappa_i + 2i(\omega - \omega_0)}{\kappa_c + \kappa_i + 2i(\omega - \omega_0)}), \tag{5.1}$$

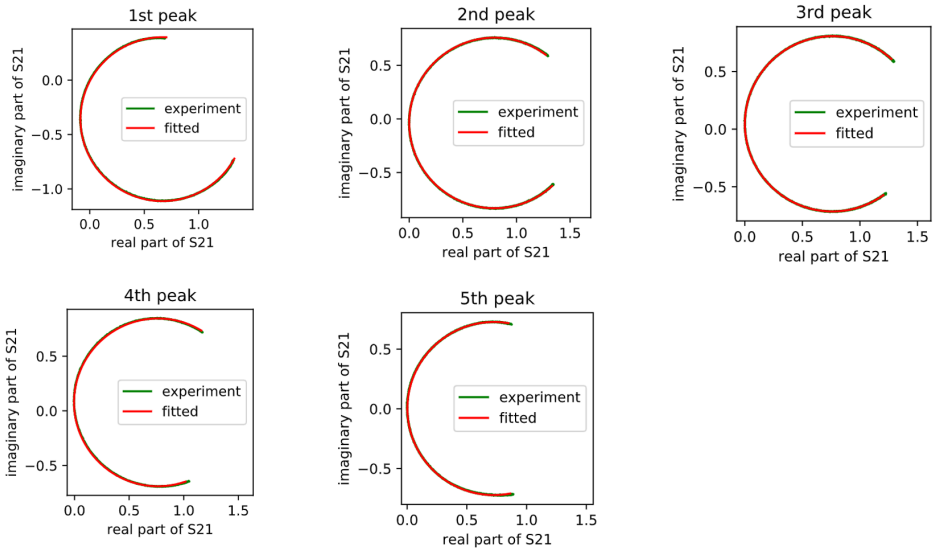

Figure 5.2.: Subfigures are the plots of the complex valued S_{21} response for each peak. The green curves display experimental data. The red curves are fits to the data. The red curves and green curves are overlap with each other, which shows fitting has high precision.

where A and ψ are the normalization amplitude and phase. κ_c is the coupling rate between the measurement pin and the electrical resonator. κ_i is the internal loss of the resonator. ω_0 is the resonance frequency of the electrical resonator. The complex phase factor of ϕ needs to be added for impedance mismatch [34, 35]. We used the least square method for the complex function to fit the data [28]. The result is shown in Fig 5.2 and Table.5.2. We can see from Fig 5.2, the fitted curve matches the experiment curve very well. From Table5.2, the R-squared value of each fitting is very close to 1, which also proves overall fitting has high precision. However, because κ_c is much bigger than κ_i (three orders of magnitudes), the relative fitting precision for κ_i is relatively low. Also for this reason we find a negative κ_i from the fit to the 4th peak. κ_c ranges from 7 MHz to 60 MHz, which is reasonable given the experience from previous simulation and

experiment construction. One source of the fitting errors is the wiggly background of the spectrum. This is because there are so many electrical elements in the setup. And these elements have their frequency response.

Comparing the resonance frequencies obtained from the fit to the simulation results, we find they differ by a few hundred MHz. The measured frequency is higher than the simulated one. The reason for this might be imperfections in the fabrication process. Concerning the fabrication process, when dicing the resonator chips, shards of the wafer may have cut through the antenna lead due to insufficient protection of the surface. This reduces the total length of the resonator and in turn, increases its resonance frequency. From the simulation, we also see the effect that if the chips are located at different places of the cavity, frequencies of the electrical resonators could also have a shift up to roughly 100 MHz.

Chip number	1	2	3	4	5
Resonator frequency($2\pi\times$GHz)	5.944	6.755	6.858	6.935	7.210
Simulation frequency($2\pi\times$GHz)	5.869	6.228	6.625	6.861	7.050
Coupling strength $\kappa_c(2\pi\times$MHz)	7.582(4)	9.380(4)	9.5288(7)	23.58(3)	62.38(5)
Internal loss $\kappa_i(2\pi\times$kHz)	31.8(2.1)	4.0(3.0)	10.3(6.0)	-12(16)	68(23)
1-R^2	9.8×10^{-5}	1.3×10^{-4}	3.1×10^{-4}	2.5×10^{-4}	2.5×10^{-4}

Table 5.2.: Fitting results

For the next step, we want to measure chips with HBAR chips to fit the values of the coupling strength between the electrical resonator and the acoustic resonator, and also the decay rate of the acoustic resonator. These two values determine how many operations could be performed in each sequence of the experiment, and also the performance of the acoustic resonator based quantum circuit, which we will discuss in the next chapter.

Chapter 6

Application of superconducting qubit and acoustic resonator coupling

In the previous part of the thesis, we introduce the hybrid quantum system of coupling qubits and acoustic resonators, and how to characterize the coupling strength and decay rate of the acoustic resonators. In this chapter, we will show one potential application of this hybrid quantum system. First, we investigate the acoustic resonator based quantum circuit in section 6.1.1 and 6.1.2. Then we compare this circuit with the traditional superconducting quantum circuit in section 6.1.3, and finally, we show a calculation of proof-of-principle experiment which we hope to implement on our system in section 6.2.

6.1. Acoustic resonator based quantum circuit

6.1.1. Introduction of acoustic resonator based quantum circuit

We can couple a superconducting qubit with a bulk acoustic wave resonator, and this technique can serve as a new tool for quantum computation. Phonon modes in acoustic resonators can have much longer coherence times than superconducting qubits, and one acoustic resonator can have many modes that can couple to a qubit. Therefore, we can use them as quantum memories to store quantum information. Here, we are going to introduce an acoustic resonator based quantum circuit (ARQC) [36, 37].

The main idea is to use a superconducting qubit as processor and phonon modes as memories for the quantum processor. Fig 6.1 shows a simple example of how a simple quantum circuit can be executed on this kind of hardware. Each phonon mode works as a quantum memory. A quantum operation is performed on the superconducting qubit and combined with swapping operations between the qubit and phonon modes. For a single qubit gate, take the example of the Hadamard gate for the first qubit. In the ARQC, we swap qubit and phonon mode 1. Then we do the Hardmard gate on the qubit and swap it back to mode 1. For a two qubit gate, take the example of a CNOT gate between qubit 1 and qubit 2. We can swap mode 1 with qubit and do a CNOT gate between the qubit and mode 2. In the end, we return the quantum state in the qubit to mode 1.

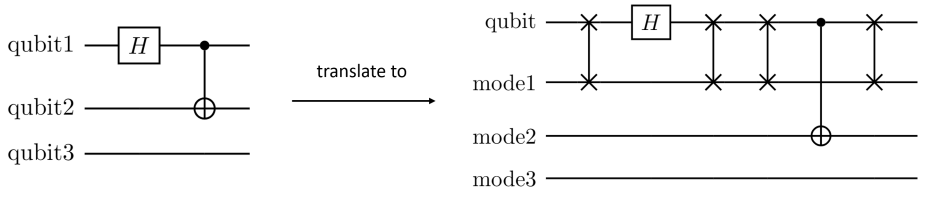

Figure 6.1.: An example of how the acoustic resonator based quantum circuit works. Left: A simple example circuit consists of a Hadamard gate and a CNOT gate. Right: By inserting swap gates between phonon modes and the qubit, we can use the qubit to execute the gates and the phonon modes as storage units for the quantum states.

6.1.2. Universal quantum gate in acoustic resonator based circuit

If we want to show an ARQC equivalent to a conventional quantum circuit, we need to prove this new circuit can operate universal quantum gates as a conventional circuit does. In the theory of quantum computing, as long as we can achieve arbitrary single quantum gates and the CNOT gate, we can implement any unitary quantum operation [4].

Right now, let's see what we have to achieve these two targets. The Hamiltonian of our system is

$$\hat{H} = \hbar\omega_q(t)\hat{a}^+\hat{a} + \frac{1}{2}\hbar\alpha\hat{a}^+\hat{a}^+\hat{a}\hat{a} + \sum_{k=1}^{n}\hbar\omega_k\hat{b}_k^+\hat{b}_k + \sum_{k=1}^{n} g_k(\hat{b}_k + \hat{b}_k^+)(\hat{a} + \hat{a}^+) + \hbar\Omega\cos(\omega_q(t))(\hat{a} + \hat{a}^+). \tag{6.1}$$

In this Hamiltonian, $\hat{a}(\hat{a}^+)$ and $\hat{b}_k(\hat{b}_k^+)$ represent the annihilation (creation) operator for the qubit and the k_{th} phonon mode. The first two terms are the energy of the superconducting qubit. α is the anharmonicity of the transmon qubit. The third term is the energy of the phonon mode. The second to last term is the coupling term between the qubit and phonon modes, where g_k is the coupling strength to the k_{th} mode. The last term represents an external drive on the qubit. Based on this Hamiltonian, we can achieve any single qubit gate on the superconducting qubit, as well as the iswap gate between the qubit and any phonon mode. The iswap gate is executed by evolving the system under the interaction term for a time of $t_{\text{swap}} = \pi/2g_k$[i]:

$$U_{\text{iswap}} = e^{-i\mathcal{H}_{\text{int}}t_{\text{iswap}}} = \begin{pmatrix} 1 & 0 & 0 & 0 \\ 0 & 0 & i & 0 \\ 0 & i & 0 & 0 \\ 0 & 0 & 0 & 1 \end{pmatrix}. \tag{6.2}$$

[i]This is the matrix if we only consider $|0\rangle$ and $|1\rangle$ state in phonon modes, if we consider more states, the matrix is shown in Appendix C

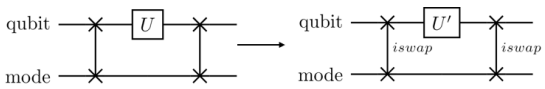

Figure 6.2.: Illustration of how to do single quantum gate on phonon mode. This equivalent only works when qubit is initialized to the ground state.

First, we will show how to achieve arbitrary single qubit gates on arbitrary phonon modes. The most intuitive way is using a swap gate to transfer the state from phonon mode to qubit, do the gate operation on the qubit and swap the state to the phonon mode. Unfortunately, we can't do a pure swap gate, we only have iswap gate between qubit and phonon mode.

As Figure.6.2 shows, if we want to do a gate represented by the unitary U on a phonon mode, we can use the iswap gate and a U'-gate on the qubit. There exists a one to one map of from the U-gate to the U'-gate.

$$U' = \begin{pmatrix} U_{11} & -iU_{12} \\ -iU_{21} & -U_{22} \end{pmatrix} \tag{6.3}$$

When we do any single qubit gate, we should make sure the qubit is initialized to the ground state. Otherwise, the phonon mode can be excited to the Fock $|2\rangle$ state and that is what we need to avoid.

After showing how to execute single qubit gates on a phonon mode, let's see how to implement the two qubit CNOT gate between phonon modes. The CNOT gate can be decomposed into a controlled phase gate (CZ gate) and single qubit gates [38]. For implementing the controlled phase gate, we need to use the qubit $|f\rangle$ state [37]. First, the qubit is initialized to its ground state, and the $|g\rangle - |e\rangle$-transition is tuned on resonance with phonon mode 1 for a time of $\pi/2g_1$, which executes an iswap gate between the qubit and mode 1. Next, the $|e\rangle - |f\rangle$-transition of the qubit is tuned on resonance with phonon mode 2 for a time of π/g_2, or two iswap gates. Phonon mode 2 acquires a π geometric phase if the qubit is in $|e\rangle$ and phonon mode 2 is in $|1\rangle$. In the end, the $|g\rangle - |e\rangle$-transition is tuned back to the energy of phonon mode 1, performing another iswap gate between the qubit and mode 1.

$$\begin{aligned}
|00g\rangle &\xrightarrow{iswap_1} |00g\rangle \xrightarrow{2*iswap_2} |00g\rangle \xrightarrow{iswap_1} |00g\rangle \\
|10g\rangle &\xrightarrow{iswap_1} i\,|00e\rangle \xrightarrow{2*iswap_2} i\,|00e\rangle \xrightarrow{iswap_1} -|10g\rangle \\
|01g\rangle &\xrightarrow{iswap_1} |01g\rangle \xrightarrow{2*iswap_2} |01g\rangle \xrightarrow{iswap_1} |01g\rangle \\
|11g\rangle &\xrightarrow{iswap_1} i\,|01e\rangle \xrightarrow{2*iswap_2} -i\,|01e\rangle \xrightarrow{iswap_1} |11g\rangle
\end{aligned} \tag{6.4}$$

Eq. (6.4) shows how the state changes with each step of the operation. In the end, only the initial state $|10\rangle$ will accumulate a π phase at the end of the operation while all the

other initial states are unaffected, executing a CZ gate.

Summarizing, we showed that the ARQC can implement arbitrary single qubit gates and two qubit CNOT gates on phonon modes. Therefore, this kind of circuit can in principle work as a general quantum circuit.

6.1.3. Comparison with traditional superconducting quantum circuits

There are some advantages for the ARQC. First, because every resonator can have tens or even hundreds of modes that couple to the qubit, it is inherently scalable. As long as we can quickly tune the qubit energy over a large range, we can use a large number of modes. Second, we can do two qubit gate between arbitrary two phonon modes. In most superconducting circuits, transmon qubits only couple to neighboring qubits. Third, phonon modes can have much longer coherence times compared with the transmon qubit, so they are very nice candidates for a quantum memory [39].

However, there are also several drawbacks of this kind of circuit. First, gates get more complicated resulting in lower fidelity. This is mainly dominated by the relatively low coupling strength between qubit and phonon mode. Second, there is some intrinsic limitation for scalability. If we want to couple too many modes, it means the energy difference between nearby mode needs to be relatively small, causing infidelity of gate operations due to parasitic couplings between the qubit and unwanted phonon modes. Third, because we only have one qubit, gates can only be performed in series, which means lower speed.

6.2. Entanglement between two phonon modes

In the last section, we showed how the ARQC functions in principle. In this section, we will show a simple proof-of-principle experiment of this kind of circuit, which generates entanglement between phonon modes and implements a tomographic measurement of two phonon modes.

The circuit for entanglement generation is shown in Fig 6.3. The qubit is initialized in the ground state and two modes are both initialized to the $|0\rangle$ state. First, we perform a π pulse on the qubit to excite it to $|e\rangle$ state. Next, we implement a square root of iswap gate between qubit and phonon mode 1 to transfer half of the excitation from qubit to mode 1. Finally, we implement an iswap gate to transfer the second half of the excitation from qubit to mode 2. At this step, the state should be $|g01\rangle + e^{i\phi}|g10\rangle$. The phase ϕ is time-dependent because the two phonon modes have different frequencies.

After generation of the entanglement, we need to measure the state of the two modes. This works via swapping the state to be measured from the phonon mode to the qubit, possibly performing single qubit rotations and measuring the qubit. To probe the state of mode 1, we first iswap the phonon state to the qubit. If we want to measure in z basis, we then directly measure the qubit state. If we want to measure in x basis, we do a $\frac{\pi}{2}$ pulse along the y-axis to qubit before the measurement. If we want to measure in y basis, we do a $\frac{\pi}{2}$ pulse along x to qubit before the measurement. The i phase caused by iswap

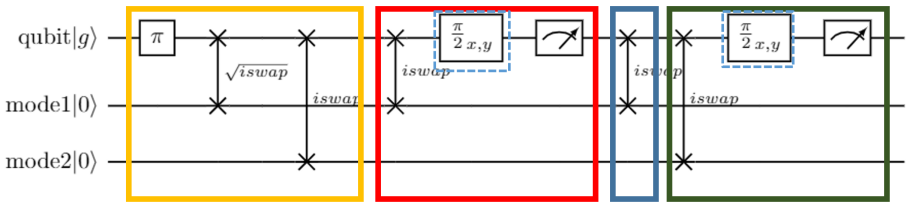

Figure 6.3.: Circuit for two modes entanglement generation. The circuit in the yellow block generates the entanglement. In the red block, the first mode is measured in x,y, or z-basis. The dashed block represents either a $\frac{\pi}{2}$ pulse along the x-axis (measurement in y basis) or along the y-axis (measurement in x basis) or no pulse (measurement in z basis). In the blue block, we remove any residual excitation from the qubit. Finally, the green block measures the second mode.

gates needs to be corrected by tuning the phase of these $\frac{\pi}{2}$ pulses. After measurement of phonon mode 1, we need another iswap gate which works as cooling down of the qubit. It is necessary because when we do an iswap gate afterward, if the qubit is beginning in an excited state, the phonon mode could transfer to the $|2\rangle$ state, which we need to avoid. After cooling down the qubit, we can do the measurement of mode 2, which is the same as the measurement of mode 1.

We performed numerical simulations of the circuit in qutip [40]. For simplicity, we only consider two phonon modes, which we manipulate in the circuit. In each phonon mode, we only consider superpositions of $|0\rangle$ and $|1\rangle$. The simulation is carried out in a rotating frame with $\omega_{rf} = (\omega_1 + \omega_2)/2$. For single qubit operations, the frequency of the qubit is tuned to the rotating frame's frequency. The parameters of the simulation are shown in Table.6.1. These parameters are based on Ref. [18] and further simulation.

phonon T_1	64 μs
phonon T_2	40 μs
qubit T_1	7 μs
qubit T_2	14 μs
phonon frequency separation $(\omega_1 - \omega_2)/2\pi$	13 MHz
bare coupling constant $g_k/2\pi$	620 kHz
Single qubit gate speed $\Omega/2\pi$	50 MHz

Table 6.1.

In the simulation, we plot the evolution of each step of the circuit, and we find some interesting phenomena that worth discussing. Fig 6.4 shows the state evolution during the $\sqrt{iswap}$ gate between the qubit and the mode 1. At the end of the gate, we can find

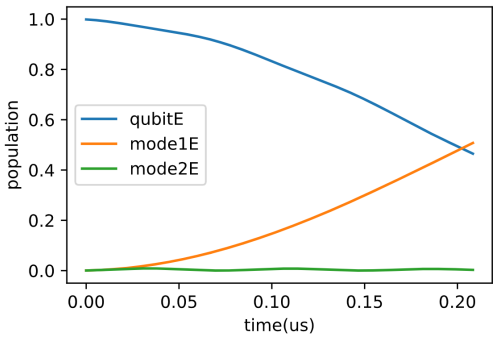

Figure 6.4.: The state evolution during the $\sqrt{iswap}$ gate between the qubit and mode 1. Blue, orange, and green curves represent the population in excited states in the qubit, mode1, and mode2 separately.

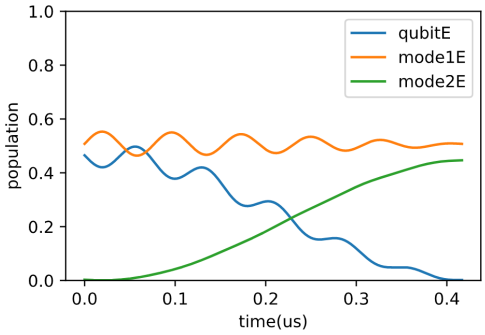

Figure 6.5.: The state evolution during the first iswap gate between the qubit and mode 1. Blue, orange, and green curves represent the population in excited states in the qubit, mode1, and mode2 separately.

that the qubit transferred half of the energy to the mode 1. However, the qubit and the mode 1 do not end at an excited state population of exactly 0.5. This is because there is already decay in the qubit. We can also see tiny oscillation of the population in phonon mode 2. Fig 6.5 shows the state evolution during the first iswap gate between the qubit and the mode 2. The qubit transfers the second half of its excitation to the phonon mode 2. We can see an unwanted phenomenon in the evolution, which is the oscillation caused by the detuned coupling between the qubit and the phonon mode 1.

Fig 6.6 shows the evolution of the detuned coupling. If the state is initialized along the z-axis of the Bloch sphere, the angle between effective coupling and state will be $\theta = \arctan\left(\frac{g}{\Delta}\right) \approx \frac{g}{\Delta}$, the approximation is because $\Delta \gg g$. Here, g represents coupling strength and Δ represents detuning frequency. The error caused by the detuned coupling is proportional to $1 - cos(2\theta) \approx \frac{2g^2}{\Delta^2}$. If, however, the initial state points along the x-axis, then the error caused by the detuned coupling is proportional to $\sin(2\theta) \approx \frac{2g}{\Delta}$. Thus, if the state is initialized along the z-axis, such as $|0\rangle$ and $|1\rangle$, the error scale caused by the detuned coupling is of second order in $\frac{g}{\Delta}$. If the state is initialized to x-y plane, such as $|0\rangle + e^{i\phi}|1\rangle$, the error scale of first order in $\frac{g}{\Delta}$. This explains why the oscillation caused by the detuned coupling is bigger when the qubit and the phonon mode are on the equator of the Bloch sphere than when they are along the z-axis of the Bloch sphere. This is an important infidelity we need to take into account and try to avoid when we design the circuit in the future.

After the generation of entanglement between the two phonon modes, we need to perform tomography of these two modes. Here, we also need the help of the qubit. Because we only use $|0\rangle$ and $|1\rangle$ of the phonon modes, the tomography procedure is

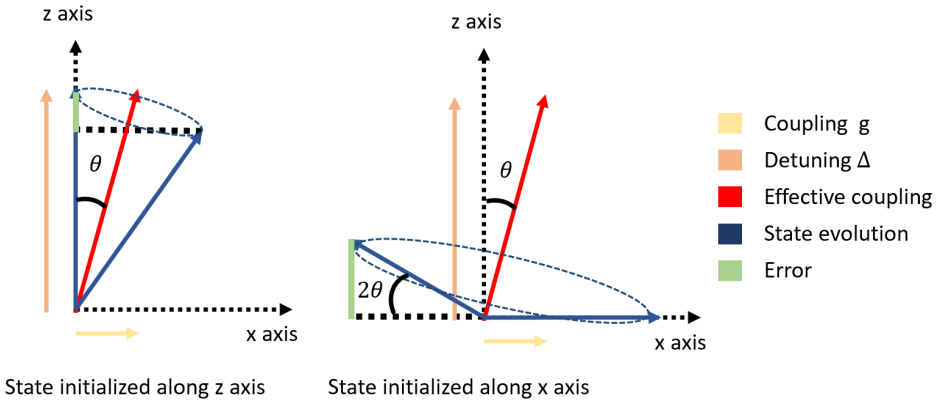

Figure 6.6.: Illustration of detuning coupling between qubit and phonon mode. Assuming we are in the rotating frame of a phonon mode detuned from the qubit. The light yellow arrow represents the coupling between qubit and phonon mode and the peach color arrow represents the detuning between the two. The sum of detuning and coupling is the effective coupling represented by the red arrow. The blue cone represents the evolution of the phonon mode that precesses around the effective coupling. The light green bar represents the error caused by this detuning coupling. The left diagram shows the state evolution, which initialized along z-axis. The right shows the same evolution but initialized along the x-axis.

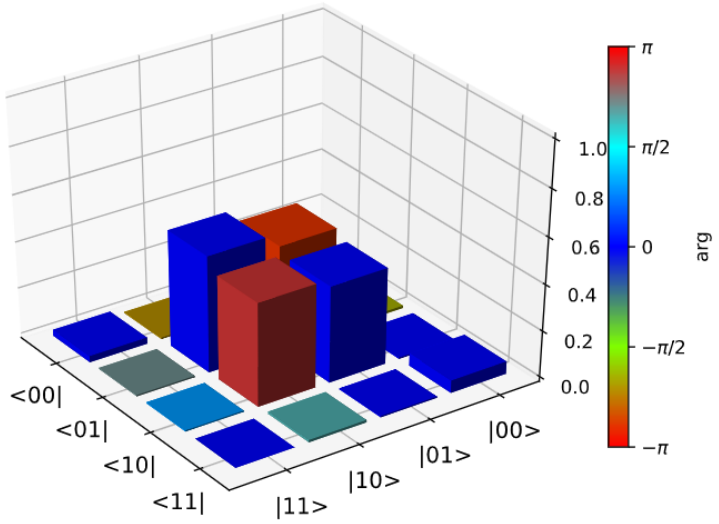

Figure 6.7.: Density matrix of the simulated measurement result. The color of each block shows the phase of the matrix term according to the color bar on the right.

the same as for a regular two qubit tomography. For two qubit tomography, we need a minimum of nine measurements of different operators of the form $\sigma_{1i} \otimes \sigma_{2j}$ $(i, j = x, y, z)$ to fully characterize the density matrix [41]. Because the two phonon modes' frequencies and single qubit operation frequency are different with each other, we need to carefully calibrate the phase of driving $\frac{\pi}{2}$ pulse when we carry out the measurement in x and y-basis. Our target state is $\frac{1}{\sqrt{2}}(|01\rangle - |10\rangle)$.

Fig 6.7 shows the density matrix based on the simulated measurement result. The simulated fidelity of the target state compared to the ideal outcome is 88.4%. In this simulation, we have taken into account the effects of qubit decay, phonon decay, phonon dephase, and detuned coupling between two phonon modes and the qubit. There are also some other effects not taken into account. In the simulation, we didn't take into account qubit dephasing channels so we just assumed $T_2 = 2T_1$ for the qubit. We also didn't take into account the readout infidelity, pulse inaccuracy, and initialization infidelity. For simplicity, we only consider two phonon modes in our simulation, so we also didn't take account coupling with other modes. For those reasons, the experimental fidelity will be a little lower than the simulated value.

From Fig 6.5 we know there is unwanted oscillation caused by detuned coupling between qubit and phonon modes. This effect will also cause the fidelity to oscillate when changing the energy difference between two phonon modes. We want to see how much infidelity is caused by the detuned coupling. As Fig 6.8 shows, the trend is such that if the energy difference between the two modes is higher, the simulated fidelity is also higher. However, we can also see the oscillation of the fidelity. This is because this energy difference determines the unwanted oscillation speed in Fig 6.5, If the unwanted oscillation ends at a different point, it can cause a different infidelity. Therefore, we

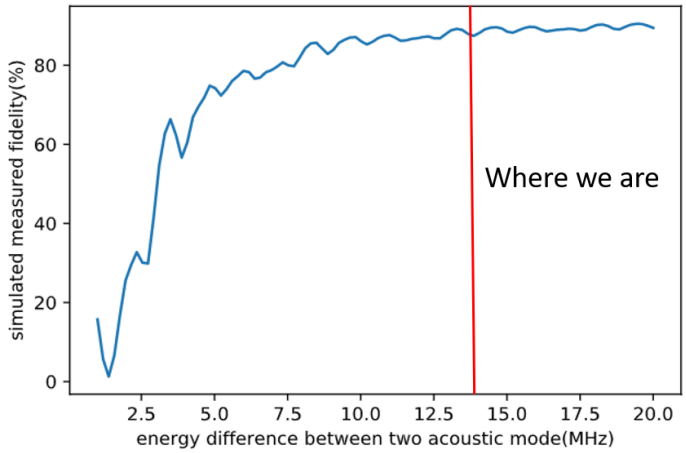

Figure 6.8.: How the fidelity changes with the energy difference between two acoustic modes

can also see the oscillation of the fidelity in Fig 6.8. In our current setup, the energy difference between the two modes is 13 MHz. According to the simulation result in Fig 6.8, the effect of the detuned coupling is almost saturated. We also simulate the case if we don't consider the effect of detuned coupling, and get the fidelity of 91.6%, which indicate the infidelity caused by the decay of the system is about 8.4%. Additionally, decay and dephasing of the phonons are much slower than the decay of the qubit. We can make the conclusion that the infidelity in our simulation is dominated by the decay of the qubit.

Chapter 7

Conclusion and Outlook

In this thesis, we have introduced how to characterize the properties of the coupling process between qubits and acoustic resonators. We started by performing input-output theory calculations for our systems and understood the relevant parameters and regimes. Then, based on simulation results, we designed the parameters of the characterization experiment. We fabricated chips and a multiplexed cavity box that holds resonators. After measuring the bare electrical resonator and analyzing the data, we find that if κ_c is much bigger than κ_i, the relative error for the fitting result of κ_i is bigger. So, if we want to measure a bare electrical resonator in the future, I suggest we design the resonator to have a smaller κ_c by changing the position of the resonator on the chip. However, if we bonded the acoustic chip and want to measure the properties of the phonon, κ_c bigger than 5 MHz is still suggested.

In chapter six we talked about a proof-of-principle experiment of the acoustic resonator based quantum circuit, which is the generation of entanglement between phonon modes. We have also shown a method to perform two-qubit gates between two phonon modes, which in itself constitutes a valuable capability in quantum architectures.

The hybrid quantum system of superconducting qubits and acoustic phonon modes also shows great potential in microwave photon to optical photon transfer. We can transfer a qubit state from qubit to phonon and also couple the laser with the photon as in traditional optomechanics. In this way, we encode the quantum information of the qubit in an optical photon. The process is in principle also reversible. As such, we can realize the remote coupling of superconducting qubits.

Our system could also be used in quantum sensing. A cat state could be generated in our system and it is sensitive to the phonon frequency. If there is force exerted on the crystal, the phonon frequency could change and be detected. So our system is also a candidate for a force sensor.

For all these proposed applications of the acoustic resonator superconducting qubit hybrids, we will want higher coupling speed and longer coherence times. Multi-layers of piezoelectrical material will provide larger coupling. A thinner acoustic resonator also has a smaller effective mode volume, thereby also increasing the coupling factor. Additionally, this would increase the free spectral range of the acoustic resonator, which improves gate fidelities at the cost of a lower number of accessible modes. Etching the curved surface on the side without the piezoelectric material of the acoustic resonator might reduce the decay rate of the phonons. In that way, the piezoelectric layer works as a flat mirror. The strain field will be perpendicular to the interface of AlN and sapphire. The energy reflected out of the phonon mode might be decreased when passing through

the interface. This might reduce the decay rate of phonons.

Appendix A

Voltage reflection coefficient

At microwave frequencies, the input signal has transmission and reflection, which is different from DC signals. Assume the incident signal is generated from a source at position $z_s < 0$, and the incident wave is $V_0^+ e^{-i\beta z}$ [23]. Suppose the reflected wave has the form $V_0^- e^{i\beta z}$. The characteristic impedance of the line is Z_0. The line is terminated by a load of Z_L. The ratio of the voltage to current on the load must be Z_L.

The total voltage of the line is the sum of the incident and reflected waves:

$$V(z) = V_0^+ e^{-i\beta z} + V_0^- e^{i\beta z}. \tag{A.1}$$

The total current on the line is the subtraction of the incident and reflected waves:

$$I(z) = \frac{V_0^+}{Z_0} e^{-i\beta z} - \frac{V_0^-}{Z_0} e^{i\beta z}. \tag{A.2}$$

At the load where $z = 0$, combining the Eqs. (A.1) (A.2), the relation of total voltage and total current is :

$$Z_L = \frac{V(z)}{I(z)} = \frac{V_0^+ + V_0^-}{V_0^+ + V_0^-} Z_0. \tag{A.3}$$

Then we can get:

$$V_0^- = \Gamma V_0^+, \Gamma = \frac{Z_L - Z_0}{Z_L + Z_0}. \tag{A.4}$$

Γ is the complex amplitude of reflected voltage normalized to the amplitude of incident voltage, which is defined as a voltage reflection coefficient.

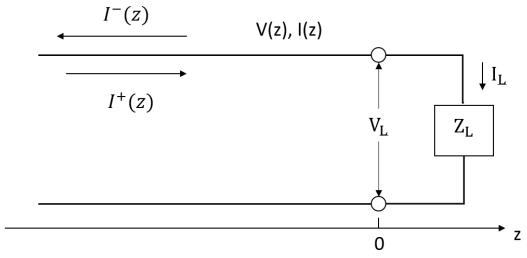

Figure A.1.: A transmission line terminated by a load

Appendix B

Scattering matrix of hanger model

Fig B.1 is the simplified circuit of the hanger model. If we look from port 1, the total load impedance is the parallel connection of Z_{total} and Z_0^{hanger}:

$$Z_{load}^{port1} = \frac{Z_{total} Z_0^{hanger}}{Z_{total} + Z_0^{hanger}}. \tag{B.1}$$

Use the voltage reflection coefficient, we can get the reflection voltage of port 1 is

$$V_1^- = \frac{Z_{load}^{port1} - Z_0^{hanger}}{Z_{load}^{port1} + Z_0^{hanger}} V_1^+. \tag{B.2}$$

Voltage on Z_{total} is V, which is equal to

$$V = V_1^+ + V_1^- = V_2^+ + V_2^-. \tag{B.3}$$

If we see from port 2, there is no incident wave in port 2. Therefore the output of port 2 V_2^- is

$$V_2^- = V_1^+ + V_1^- = \frac{Z_{total}}{Z_{total} + \frac{Z_0^{hanger}}{2}} V_1^+. \tag{B.4}$$

Then we can get the scattering matrix term S_{21} for hanger model:

$$S_{21} = \frac{V_2^-}{V_1^+}|_{V_2^+=0} = \frac{Z_{total}}{Z_{total} + \frac{Z_0^{hanger}}{2}}. \tag{B.5}$$

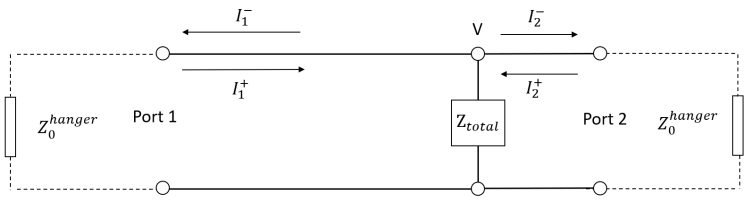

Figure B.1.: Circuit diagram of hanger model

Appendix C

Matrix representation of iswap gate

If we consider the Hilbert space of the phonon modes up to Fock $|2\rangle$ state,

$$\hat{H} = \hbar g_k(\hat{a}\hat{b}^+ + \hat{a}^+\hat{b}) = \hbar g_k \begin{pmatrix} 0 & 0 & 0 & 0 & 0 & 0 \\ 0 & 0 & 0 & 1 & 0 & 0 \\ 0 & 0 & 0 & 0 & \sqrt{2} & 0 \\ 0 & 1 & 0 & 0 & 0 & 0 \\ 0 & 0 & \sqrt{2} & 0 & 0 & 0 \\ 0 & 0 & 0 & 0 & 0 & 0 \end{pmatrix} \begin{matrix} |g,0\rangle \\ |g,1\rangle \\ |g,2\rangle \\ |e,0\rangle \\ |e,1\rangle \\ |e,2\rangle \end{matrix}, \tag{C.1}$$

where $\hat{a}^+$ ($\hat{a}$), $\hat{b}^+$ ($\hat{b}$) represents creation (annihilation) operator of the qubit and phonon respectively. The iswap gate is executed by evolving the system under the interaction term for a time of $t_{\text{swap}} = \pi/2g_k$. The unitary matrix for this operation is

$$U_{iswap} = \begin{pmatrix} 1 & 0 & 0 & 0 & 0 & 0 \\ 0 & 0 & 0 & i & 0 & 0 \\ 0 & 0 & -0.606 & 0 & 0.796i & 0 \\ 0 & i & 0 & 0 & 0 & 0 \\ 0 & 0 & 0.796i & 0 & -0.606 & 0 \\ 0 & 0 & 0 & 0 & 0 & 1 \end{pmatrix} \begin{matrix} |g,0\rangle \\ |g,1\rangle \\ |g,2\rangle \\ |e,0\rangle \\ |e,1\rangle \\ |e,2\rangle \end{matrix}. \tag{C.2}$$

We can see from Eq. (C.2), in the iswap operation, state $|e,1\rangle$ can transfer population to state $|g,2\rangle$, which is out of our computation basis. Therefore before very iswap operation in ARQC, we need to guarantee at most one excitation in the qubit and the phonon modes. This is also the reason we cool down the qubit before the iswap operation.

Bibliography

1. Moore, G. E. Cramming more components onto integrated circuits. *Proceedings of the IEEE* **86,** 82–85 (1998).
2. Theis, T. N. & Wong, H.-S. P. The end of moore's law: A new beginning for information technology. *Computing in Science & Engineering* **19,** 41–50 (2017).
3. Shor, P. W. *Algorithms for quantum computation: discrete logarithms and factoring* in *Proceedings 35th Annual Symposium on Foundations of Computer Science* (1994), 124–134.
4. Nielsen, M. A. & Chuang, I. *Quantum computation and quantum information* 2002.
5. Clarke, J. & Wilhelm, F. K. Superconducting quantum bits. *Nature* **453,** 1031–1042 (2008).
6. Häffner, H., Roos, C. F. & Blatt, R. Quantum computing with trapped ions. *Physics reports* **469,** 155–203 (2008).
7. Loss, D. & DiVincenzo, D. P. Quantum computation with quantum dots. *Physical Review A* **57,** 120 (1998).
8. Cory, D. G., Fahmy, A. F. & Havel, T. F. Ensemble quantum computing by NMR spectroscopy. *Proceedings of the National Academy of Sciences* **94,** 1634–1639 (1997).
9. Childress, L. & Hanson, R. Diamond NV centers for quantum computing and quantum networks. *MRS bulletin* **38,** 134–138 (2013).
10. Mayers, D. Unconditional security in quantum cryptography. *Journal of the ACM (JACM)* **48,** 351–406 (2001).
11. Liao, S.-K. *et al.* Satellite-to-ground quantum key distribution. *Nature* **549,** 43–47 (2017).
12. Liao, S.-K. *et al.* Satellite-relayed intercontinental quantum network. *Physical review letters* **120,** 030501 (2018).
13. Ren, J.-G. *et al.* Ground-to-satellite quantum teleportation. *Nature* **549,** 70 (2017).
14. Degen, C. L., Reinhard, F. & Cappellaro, P. Quantum sensing. *Reviews of modern physics* **89,** 035002 (2017).
15. DiVincenzo, D. P. The physical implementation of quantum computation. *Fortschritte der Physik: Progress of Physics* **48,** 771–783 (2000).
16. Xiang, Z.-L., Ashhab, S., You, J. & Nori, F. Hybrid quantum circuits: Superconducting circuits interacting with other quantum systems. *Reviews of Modern Physics* **85,** 623 (2013).
17. Chu, Y. *et al.* Quantum acoustics with superconducting qubits. *Science* **358,** 199–202 (2017).

18. Chu, Y. *et al.* Creation and control of multi-phonon Fock states in a bulk acoustic-wave resonator. *Nature* **563,** 666–670 (2018).
19. Walls, D. F. & Milburn, G. J. *Quantum optics* (Springer Science & Business Media, 2007).
20. Ford, G. W., Lewis, J. T. & O'connell, R. Quantum langevin equation. *Physical Review A* **37,** 4419 (1988).
21. Axline, C. J. *Building Blocks for Modular Circuit QED QuantumComputing* PhD thesis (Yale University, 2018).
22. Geerlings, K. L. *Improving coherence of superconducting qubits and resonators* (Yale University, 2013).
23. Pozar, D. M. *Microwave Engineering 3e* (Wiley, 2006).
24. Koch, J. *et al.* Charge-insensitive qubit design derived from the Cooper pair box. *Physical Review A* **76,** 042319 (2007).
25. Royer, D. & Dieulesaint, E. *Elastic waves in solids I: Free and guided propagation* (Springer Science & Business Media, 1999).
26. Cleland, A. N. *Foundations of nanomechanics: from solid-state theory to device applications* (Springer Science & Business Media, 2013).
27. Chu, Y. *Lecture notes in Quantum Acoustics and Optomechanics* Feb. 2020.
28. Virtanen, P. *et al.* SciPy 1.0: Fundamental Algorithms for Scientific Computing in Python. *Nature Methods* **17,** 261–272 (2020).
29. Wang, C. *et al.* Surface participation and dielectric loss in superconducting qubits. *Applied Physics Letters* **107,** 162601 (2015).
30. Jaeger, R. C. *Introduction to microelectronic fabrication* (Prentice Hall Upper Saddle River, NJ, 2002).
31. Kharel, P. *et al.* Ultra-high-Q phononic resonators on-chip at cryogenic temperatures. *APL Photonics* **3,** 066101 (2018).
32. Kittel, C., McEuen, P. & McEuen, P. *Introduction to solid state physics* (Wiley New York, 1996).
33. Krinner, S. *et al.* Engineering cryogenic setups for 100-qubit scale superconducting circuit systems. *EPJ Quantum Technology* **6,** 2 (2019).
34. Khalil, M., Stoutimore, M., Wellstood, F. & Osborn, K. An analysis method for asymmetric resonator transmission applied to superconducting devices. *Journal of Applied Physics* **111,** 054510 (2012).
35. Probst, S., Song, F., Bushev, P., Ustinov, A. & Weides, M. Efficient and robust analysis of complex scattering data under noise in microwave resonators. *Review of Scientific Instruments* **86,** 024706 (2015).

36. Pechal, M., Arrangoiz-Arriola, P. & Safavi-Naeini, A. H. Superconducting circuit quantum computing with nanomechanical resonators as storage. *Quantum Science and Technology* **4,** 015006 (2018).

37. Naik, R. *et al.* Random access quantum information processors using multimode circuit quantum electrodynamics. *Nature communications* **8,** 1–7 (2017).

38. Cirac, J. I. & Zoller, P. Quantum computations with cold trapped ions. *Physical review letters* **74,** 4091 (1995).

39. Hann, C. T. *et al.* Hardware-efficient quantum random access memory with hybrid quantum acoustic systems. *Physical Review Letters* **123,** 250501 (2019).

40. Johansson, J. R., Nation, P. D. & Nori, F. QuTiP 2: A Python framework for the dynamics of open quantum systems. *Computer Physics Communications* **184,** 1234–1240 (2013).

41. Liu, Y.-x., Wei, L. & Nori, F. Tomographic measurements on superconducting qubit states. *Physical Review B* **72,** 014547 (2005).